Available online at www.sciencedirect.com

ScienceDirect

Underground Space 25 (2025) 74–98

www.keaipublishing.com/undsp

Research Paper

Progressive failure of water-filled karst cave of stratified tunnel using coupled discontinuous smoothed particle hydrodynamics method

Chengzhi Xia [a,b], Zhenming Shi [a,b], Liu Liu [c], Guangyin Lu [e], Lin Zhou [a], Chuanyi Tao [e], Shaoqiang Meng [a,b,d,*]

[a] College of Civil Engineering, Tongji University, Shanghai 200092, China
[b] Key Laboratory of Geotechnical and Underground Engineering of Ministry of Education, Tongji University, Shanghai 200092, China
[c] State Key Laboratory of Geomechanics and Geotechnical Engineering, Institute of Rock and Soil, Mechanics, Chinese Academy of Sciences, Wuhan 430071, China
[d] Shanghai Research Institute for Intelligent Autonomous Systems, Tongji University, Shanghai 200092, China
[e] School of Geoscience and Info-physics, Central South University, Changsha 410083, China

Received 24 March 2024; received in revised form 26 May 2024; accepted 11 October 2024
Available online 26 August 2025

Abstract

Tunnel construction in karst terrain is influenced by water-filled karst caves and stratigraphic layers, which involves failure characteristics of water-resistant structures and complex fluid–solid interaction (FSI) processes. To cope with this challenge, this paper used coupled discontinuous smoothed particle hydrodynamics (CDSPH) method for investigating water inrush of tunnels considering stratigraphic layers and karst cave positions. Hydraulic fracturing test and sliding induced impulsive wave test were carried out to verify the accuracy of the CDSPH method. Moreover, a comprehensive analysis of inrush events in the field-scale Qiyeshan (QYS) karst tunnel was conducted, considering different layer dip angles and cave positions on the evolution characteristics of inrush disasters, with quantitative parameters proposed for predicting water/mud inrush from local to overall disaster. The simulation results indicate that CDSPH karst model has been verified to faithfully capture the progressive failure of water-resistant structure during inrush in stratigraphic layers. Water/mud inrush in QYS tunnels can be divided into four stages based on vertical/horizontal stress characteristics, encompassing hydraulic fracturing of karst caves, local inrush, rock collapse, and overall inrush. The dip angle of the bedding planes affects the hydraulic failure characteristics of karst caves. When the cave is located at the top of the tunnel, the water-resistant structures with a dip angle (θ) of 45° poses the highest risk, while $\theta = 0°$ provides the most stability. Furthermore, the decrease in water pressure and the occurrence of the maximum flow velocity within the cave can serve as vital indexes to predict the transition from local inrush to overall inrush disaster. These findings emphasize the importance of the CDSPH tunnel model considering stratigraphic layers and karst cave positions when predicting water/mud inrush, and provide guidance for the prevention of inrush flow in karst tunnels.

Keywords: Coupled discontinuous smoothed particle hydrodynamics; Stratigraphic layers; Rock tunnel; Water inrush; Karst cave

1 Introduction

In the karst strata, pre-existing discontinuities such as flaws, cracks, joint sets, bedding, blocks and fault are quite widespread and are always developed inside the water/mud resistant rock mass (Peng et al., 2022). The construction of numerous karst tunnels has revealed that instability and collapse of water-resistant structures between the excavation opening and the concealed karst cave are the most common engineering problems in karst areas (Williams, 2008), particularly for filling-type karst caves (Qian & Lin, 2016). Moreover, the pre-existing bedding feature in karst areas not only affects the surface water supply but

* Corresponding author at: College of Civil Engineering, Tongji University, Shanghai 200092, China.
E-mail address: 2211051@tongji.edu.cn (S. Meng).
Peer review under the responsibility of Tongji University

https://doi.org/10.1016/j.undsp.2024.10.006

Nomenclature

c_0	Numerical speed of sound
$\boldsymbol{F}_i^{\mathrm{cn}}$	Normal contact force
$\boldsymbol{F}_i^{\mathrm{cs}}$	Shear contact force
$\{\boldsymbol{F}_i^{\mathrm{cs}}\}_{\mathrm{update}}$	Modified shear contact force
$\boldsymbol{f}_{\mathrm{F}}^{\mathrm{d}}$	Interaction forces exerted on the fluid particles due to the neighbouring discontinuous particle
$\boldsymbol{f}_{\mathrm{d}}^{\mathrm{F}}$	Interaction forces exerted on the discontinuous particle due to the neighbouring fluid particles
$\boldsymbol{f}_{\mathrm{s}}^{\mathrm{F}}$	Interaction force exerted on the solid particle due to the neighbouring fluid particles
$\boldsymbol{f}_{\mathrm{F}}^{\mathrm{S}}$	Interaction force exerted on the fluid particle due to the neighbouring solid particles
$\boldsymbol{f}^{\alpha}$	External force
G_{r}	Shear modulus of rock
$\boldsymbol{g}$	Acceleration of gravity
h	Smoothing kernel radius
K	Bulk modulus
k_{n}	Normal stiffness
k_{s}	Shear stiffness
m	Mass
m^{h}	Shape parameter
$\boldsymbol{n}$	Unit vector in the direction normal to the relative velocity
P_{r}	Pressure of rock particles
P_{ω}	Hydrostatic pressure of fluid particles
$\boldsymbol{R}_{\mathrm{r}}^{\alpha\beta}$	Rotation rate tensor of rock particles
r_0	Cut off radius
$\boldsymbol{S}_{\mathrm{r}}^{\alpha\beta}$	Deviatoric stress of rock particles
$\boldsymbol{S}_{\omega}^{\alpha\beta}$	Deviatoric stress of fluid particles
$\boldsymbol{T}$	Artificial stress
t	Calculation time
U	Intact particle ensemble
U^{n}	Penetration of the particle influence domain 、
$\boldsymbol{v}$	Velocity vector
W	Kernel function
$\boldsymbol{x}$	Spatial coordinate vector
$\mathfrak{R}$	Damaged particle ensemble
$\mathfrak{R}_{ij}$	Kernel functions
μ_{r}	Diffusive coefficient
$\delta^{\alpha\beta}$	Kronecker delta
$\boldsymbol{\varepsilon}_{\mathrm{r}}^{\alpha\beta}$	Strain rate tensor of rock particles
$\boldsymbol{\varepsilon}_{\mathrm{r}}^{\gamma\gamma}$	Volumetric strain rate of rock particles
$\boldsymbol{\varepsilon}_{\omega}^{\alpha\beta}$	Shear strain rate of fluid particles
μ_{ω}	Viscosity of fluid particles
μ^{fric}	Friction coefficient between the sliding surface and the sliding block
ρ	Density
ρ_0	Initial density
$\boldsymbol{\sigma}$	Cauchy stress tensor
χ	Constant coefficient
ψ	Fracture sign
θ	Dip angle
$\boldsymbol{\Pi}$	Artificial viscosity
ΔP	Initial particle spacing
ΔU^{s}	Relative velocity between two particles
$\partial\mathfrak{R}_{ij}$	Kernel functions gradient
∂W	Kernel function gradient

also has a great impact on the stability of the aquifer between karst caves and excavation faces (Li et al., 2018). Figure 1 illustrates the general conditions leading to sudden water inrush in karst geomorphology due to excavation, typically considering the impact of both stratified formations and high-pressure concealed cave. The specific performance is the mechanical transverse isotropy of these bedding planes, combined with the uncertain position of concealed karst caves, which often degrades strength of rock mass and imposes significant influences on the crack propagation mechanism, thereby resulting in catastrophic inrush disasters. For example, obvious water bursting on the left wall of YK19 + 888 in the tunnel linings of Qiyueshan with stratified structure is observed (Wang et al., 2019). Currently, the mechanical mechanism of the rock failure and water inrush in stratified karst tunnels remains unclear. Therefore, a quantitative investigation of the effort of bedding plane properties of water-resistant rock on water inrush in karst tunnels is of great significance for accurately preventing water/mud inrush and for post-disaster management of water gushing in tunnels.

The research on the water inrush and progressive failure of stratified karst tunnels mainly focuses on experimental investigations, numerical simulations, and theoretical analyses. Experimental studies have been widely recognized as the most direct approach to understanding the rupture and instability processes of water-resistant structures when the tunnel face is near high-pressure karst cave. Large-scale geomechanics model tests have revealed critical waterproof-resistant thickness on the inrush accident (Jiang et al., 2017), the catastrophic mechanisms of water inrush in closed karst caves during shield excavation (Li et al., 2020), and the criteria for water inrush with respect to displacement and water pressure (Liang et al., 2016). Despite the limited number of monitoring components and the functional limitations of monitoring instruments, these experiments have successfully quantified macro information on water inrush. Theoretical research has relied on laboratory observations to summarize the mechanical laws and quantify the mechanical characteristics of stratified rocks adjacent to high-pressure karst structures. For instance, the calculation of the water inrush criterion under seismic effects (Yan et al., 2006) and the minimum rock layer thickness between the working face and the cavern under static effects (Wu et al., 2019) have been researched using representative mechanical models. However, theoret-

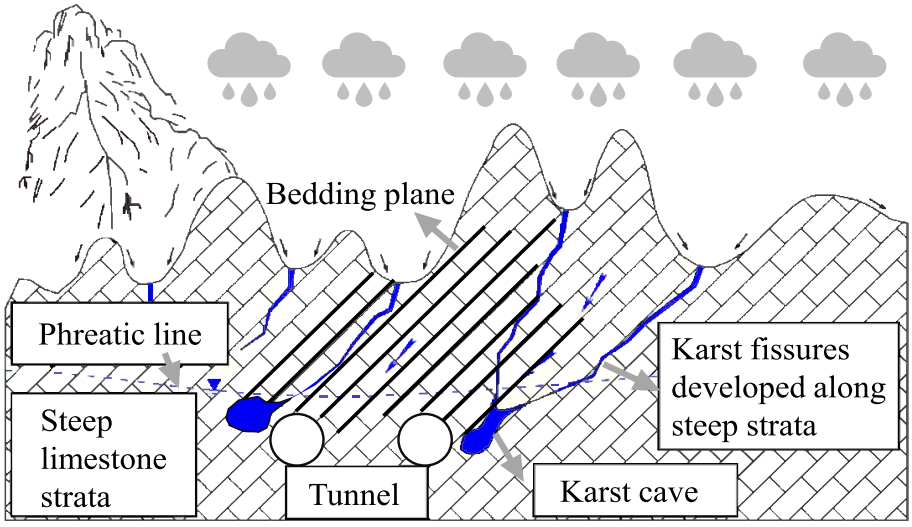

Fig. 1. Geological model of water-filled karst cave of stratified tunnels in karst area and cases of water inrush of stratified rock tunnel structures.

ical methods cannot adequately consider the bedding plane properties of rock strata and the variation of water pressure with time within concealed karst caves.

Fortunately, the numerical simulation method can solve the aforementioned limitation, and it has the function of visualizing the dynamic water inrush rupture process and progressive failure (cracking and contact) of the water-resistant structures. For instance, finite element method (FEM) (Zhu & Wei, 2011) and material point method (Wang et al., 2020) are adopted widely in the analysis of various water inrush accidents. Comparatively, discontinuous deformation analysis (DDA) (Peng et al., 2022) and discrete element method (DEM) (Zhou et al., 2020) are more suitable for analyzing the detailed volution of disaster in heterogeneous strata. However, these methods are limited in their ability to model the fluid phase and investigate catastrophic mechanisms of inrush disasters. Therefore, computational fluid dynamics (CFD) (Cui et al., 2020; Xie et al., 2023; Zhang et al., 2019) or lattice Boltzmann method (LBM) (Jin et al., 2021) based on pipe-flow and non-Darcian seepage theories have been increasingly adopted to accurately capture the fluid dynamics and catastrophic mechanisms associated with inrush disasters. However, modeling complex failure behavior and fracture propagation mechanism by CFD or LBM is still challenging without coupling other solid solvers.

Smoothed particle hydrodynamics (SPH) (Lucy, 1977) has emerged as a versatile tool for simulating fluids and fluid-like materials over last decade (Bui et al., 2009, 2008; Gui et al., 2015; Lian et al., 2023). In recent years, it has been widely used to model the fluid component in water inrush scenarios by coupling with other solid solvers. For instance, Wang et al. (2020) adopted a coupled FEM and SPH method to simulate the damage to barrier walls and water inrush caused by artificial excavation disturbances. In their study, the FEM and SPH models represented rock wall and water, respectively. Peng et al. (2022) employed a coupled DDA and SPH method to simulate water inrush during tunnel construction. In their study, the DDA and SPH models represented rock and water, respectively. The above studies have typically treated SPH as a fluid and employed other solid solvers to simulate rock failure, which not only increased the complexity of programming but also introduced more artificial assumptions at the coupling interface of solid and fluid, thereby reducing the efficiency of calculations.

To address this defect, several researchers have proposed transforming the constitutive behavior of SPH particles from fluid-like to solid-like (Gray & Monaghan, 2004; Monaghan, 2000). SPH is capable of modeling complex failure behavior and fracture propagation mechanism by introducing appropriate fracture criteria. For example, Mu et al. (2022) developed damage models for rock masses based on sewerage and thermal fields, as well as considering friction effects, and applied and validated them in jointed rock masses. Xia et al. (2022) applied an modified SPH method to reproduce fracture process of a stratified rock cell and tunnel. Yu et al. (2021) developed an improved kernel of smoothed particle hydrodynamics (IKSPH) method to investigate the cracking processes in rock tunnels under mechanical loading. Additionally, other damaged frameworks in SPH were also developed for modeling failure behavior and fracture propagation mechanism (Bi & Zhou, 2015; Zhou et al., 2018, 2016, 2015a) However, block contact of fracture surface has been absent from the aforementioned studies, and no literature has yet been reported the implementation of contact and sliding processes after rock fracture based on SPH framework, which limits the simulation of complete failure in tunnels using SPH. Furthermore, to date, there has been a lack of appropriate fluid–solid interaction (FSI) framework to reproduce the water inrush in the tunnel considering cracking and contact of rock. In particular, the framework is capable of considering the complex interaction of rock and inrush.

Considering the aforementioned limitations, the coupled discontinuous smoothed particle hydrodynamics (CDSPH) method is employed in this study to explore the progressive failure, complex interaction between pre-existing water-resistant structures and water/mud inrush scenarios within the Qiyueshan (QYS) tunnel, a rock karst tunnel prototype with varying dip angles (θ) of the stratigraphic layer and cave positions. This investigation encompasses the displacement, stress, damage characteristics of the underlying rocks, as well as the flow velocity and dynamic water pressure associated with the inrush event. Essential metrics are extracted to anticipate the shift from localized inrush incidents to overall inrush disasters, aiding practical monitoring. The subsequent sections delineate: Section 2 introduces the fundamental principles of the CDSPH method. Section 3 validates its effectiveness in addressing cracking, contact, and fluid–structure interaction through hydraulic fracturing tests, flume experiments, and numerical simulations. Section 4 encompasses a comprehensive analysis of a real QYS tunnel inrush incident involving stratified rock karst tunnels with varying dip angles (θ) and cave positions. Finally, discussions center around the pivotal role of water pressure and flow velocity in predicting the state of water/mud inrush and outline the strengths and limitations of the CDSPH tunnel model.

2 Numerical simulation method

2.1 Discretization of governing equations

The foundation of CDSPH method is SPH. The SPH method is a powerful meshless technique that possesses the capability of simulating both fluids and solids under a unified framework based on Lagrangian formulations (Gray & Monaghan, 2004). The conservation equations for mass and momentum in fluids and solids, with isentropic or isothermal equations of state, are of paramount importance (Gray et al., 2001). For convenience of explanation, a and b, i and j are marked as base and adjacent particle of water and rock, respectively. For density discretization, rocks and water are basically based on different discretization equations, and they can be defined by

$$\frac{\mathrm{d}\rho_i}{\mathrm{d}t} = \rho_i \sum\nolimits_j \frac{m_j}{\rho_j}\left(\boldsymbol{v}_i^{\beta} - \boldsymbol{v}_j^{\beta}\right) W_{ij,\beta}, \tag{1}$$

$$\begin{aligned}\frac{\mathrm{d}\rho_a}{\mathrm{d}t} = {} & \sum\nolimits_{b=1}^{N} m_b\left(\boldsymbol{v}_a^{\alpha} - \boldsymbol{v}_b^{\alpha}\right)\frac{\partial W_{ab}}{\partial \boldsymbol{x}_a^{\alpha}} \\ & + 0.2Hc_0\sum\nolimits_{b=1}^{N}\left(\frac{\rho_a}{\rho_b} - 1\right) \\ & \times \frac{1}{\left(\boldsymbol{x}_a^{\alpha} - \boldsymbol{x}_b^{\alpha}\right) + 0.01H^2} m_j\left(\boldsymbol{x}_a^{\alpha} - \boldsymbol{x}_b^{\alpha}\right)\frac{\partial W_{ab}}{\partial \boldsymbol{x}_a^{\alpha}},\end{aligned} \tag{2}$$

where ρ denotes the density of SPH particles; $\boldsymbol{v}$ and $\boldsymbol{x}$ are the velocity vector and spatial coordinate vector, respectively; α and β refer to Cartesian components x and y, subject to Einstein summation convention in two dimensions (Gray & Monaghan, 2004); m represents the mass; t denotes calculation time. c_0 is a numerical speed of sound; The former calculates rock, and the latter calculates water based on density correction; W and ∂W are the kernel function and its gradient, respectively. H denotes the depth of the fluid domain. The cubic form (Vacondio et al., 2013) is adopted in this study. N denotes the total number of particles; However, there are some differences between rock and water in the dispersion of velocity. For water velocity, it can be defined by

$$\frac{\mathrm{d}\boldsymbol{v}_a^{\alpha}}{\mathrm{d}t} = \sum\nolimits_{b=1}^{N} m_b\left(\frac{\boldsymbol{\sigma}_a^{\alpha\beta}}{\rho_a^2} + \frac{\boldsymbol{\sigma}_b^{\alpha\beta}}{\rho_b^2} + \boldsymbol{\Pi}_{ab}\right)\frac{\partial W_{ab}}{\partial \boldsymbol{x}_a^{\alpha}} + \frac{\boldsymbol{f}_a^{\alpha}}{m_a}, \tag{3}$$

where $\boldsymbol{\Pi}$ denotes the artificial viscosity (Monaghan, 2005). Cauchy stress tensor $\boldsymbol{\sigma}$ is caculated as $\boldsymbol{\sigma}^{\alpha\beta} = -P\delta^{\alpha\beta} + \boldsymbol{S}^{\alpha\beta}$, and $\delta^{\alpha\beta}$ denotes the Kronecker delta (Gray et al., 2001). For fluid phases, the hydrostatic pressure P_ω can be determined using an equation of state (EOS), Molteni and Colagrossi (2009) expressed as $P_\omega = \frac{c_0^2\rho_0}{7}\left[\left(\frac{\rho}{\rho_0}\right)^7 - 1\right]$. c_0 is the numerical speed of sound and the value is determined according to Molteni and Colagrossi (2009). Deviatoric stress $\boldsymbol{S}_\omega^{\alpha\beta}$ are objectively proportional to the shear strain rate $\boldsymbol{\varepsilon}_\omega^{\alpha\beta}$ and viscosity μ_ω, i.e., $\boldsymbol{S}_\omega^{\alpha\beta} = \mu_\omega\boldsymbol{\varepsilon}_\omega^{\alpha\beta}$, and μ_ω is adopted as 1×10^{-3} m^2/s according to Gomez-Gesteira et al. (2012). $\boldsymbol{f}^{\alpha}$ is an external force. For the dispersion of rock mass velocity, it described as follows:

$$\frac{\mathrm{d}\boldsymbol{v}_i^{\alpha}}{\mathrm{d}t} = \sum\nolimits_{j=1}^{N} m_j\left(\frac{\boldsymbol{\sigma}_i^{\alpha\beta}}{\rho_i^2} + \frac{\boldsymbol{\sigma}_j^{\alpha\beta}}{\rho_j^2} + \boldsymbol{\Pi}_{ij} - \boldsymbol{T}_{ij}\right)\frac{\partial W_{ij}}{\partial \boldsymbol{x}_i^{\alpha}} + \frac{\boldsymbol{f}_i^{\alpha}}{m_i}, \tag{4}$$

where $\boldsymbol{T}$ denotes artificial stress (Monaghan, 2005). For rock, the pressure P_r can be determined using a linear equation of state which obeys Hooke's law (Monaghan, 2005) and it is determined by $P_\mathrm{r} = K\left(\frac{\rho}{\rho_0} - 1\right)$, K denotes bulk modulus, and the deviatoric stress of rock $\boldsymbol{S}_\mathrm{r}^{\alpha\beta}$ is objectively obtained from the material frame indifferent Jaumann rate (Monaghan, 2005).

Moreover, for solving the internal force, there are differences between rock and water in the dispersion of $\boldsymbol{S}_a^{\alpha\beta}$. For the dispersion of viscous shear stress $\boldsymbol{S}_a^{\alpha\beta}$ in water domain, it can be described as follows:

$$\begin{aligned}\boldsymbol{S}_a^{\alpha\beta} = {} & \mu_\mathrm{r}\sum\nolimits_b \frac{m_b}{\rho_a}\left(\boldsymbol{v}_a^{\alpha} - \boldsymbol{v}_b^{\alpha}\right) W_{ab,\beta} \\ & + \sum\nolimits_b \frac{m_b}{\rho_b}\left(\boldsymbol{v}_a^{\beta} - \boldsymbol{v}_b^{\beta}\right) W_{ab,\alpha} - \left[\frac{2}{3}\sum\nolimits_b\left(\boldsymbol{v}_a^{\gamma} - \boldsymbol{v}_b^{\gamma}\right) W_{ab,\gamma}\right]\delta^{\alpha\beta},\end{aligned} \tag{5}$$

where μ_r is the diffusive coefficient, whose value is 0.1 here according to Molteni and Colagrossi (2009). For the dispersion of deviatoric stress $\boldsymbol{S}_i^{\alpha\beta}$ in rock domain, it can be defined by

$$\frac{\mathrm{d}\boldsymbol{S}_i^{\alpha\beta}}{\mathrm{d}t} = -G_\mathrm{r}\sum_j \frac{m_j}{\rho_j}\left[\left(\boldsymbol{v}_i^\alpha - \boldsymbol{v}_j^\alpha\right)W_{ij,\beta} + \left(\boldsymbol{v}_i^\beta - \boldsymbol{v}_j^\beta\right)W_{ij,\alpha} - \frac{1}{3}\left(\boldsymbol{v}_i^\gamma - \boldsymbol{v}_j^\gamma\right)W_{ij,\gamma}\right] + \boldsymbol{S}_{ri}^{\gamma\beta}\boldsymbol{R}_i^{\alpha\gamma} + \boldsymbol{S}_{ri}^{\alpha\gamma}\boldsymbol{R}_i^{\beta\gamma}, \tag{6}$$

where G_r represents shear modulus of rock. $\boldsymbol{\varepsilon}_\mathrm{r}^{\gamma\gamma}$ is volumetric strain rate of rock. $\boldsymbol{\varepsilon}_\mathrm{r}^{\alpha\beta}$ and $\boldsymbol{R}_\mathrm{r}^{\alpha\beta}$ denote strain and rotation rate tensor of rock, respectively. γ refers to Cartesian components x and y, subject to Einstein summation convention in two dimensions (Gray & Monaghan, 2004).

2.2 Coupled contact and cracking of rock

To address the cracking behavior of rock, the Mohr–Coulomb criterion with tensile truncation was adopted to determine the initiation and propagation of cracks (Xia et al., 2024c, 2023). To account for the failure of base particles, a fracture sign ψ is introduced into the kernel function derivative. When failure occurs, $\psi = 0$, signifying the breakage of the virtual bond (kernel) between the original particles and the generation of a crack. Otherwise, $\psi = 1$. The kernel function derivative of damaged particles and damage control equation are defined as follows:

$$\frac{\partial \mathfrak{R}_{ij}}{\partial \boldsymbol{x}_i} = \psi\frac{\partial W_{ij}}{\partial \boldsymbol{x}_i}, \tag{7}$$

$$\begin{cases} \frac{\mathrm{d}\rho_i}{\mathrm{d}t} = \sum_{j\in U} m_j\left(\boldsymbol{v}_i^\alpha - \boldsymbol{v}_j^\alpha\right)\frac{\partial W_{ij}}{\partial \boldsymbol{x}_i^\alpha} + \sum_{j\in\mathfrak{R}} m_j\left(\boldsymbol{v}_i^\alpha - \boldsymbol{v}_j^\alpha\right)\frac{\partial \mathfrak{R}_{ij}}{\partial \boldsymbol{x}_i^\alpha} \\ \frac{\mathrm{d}\boldsymbol{v}_i^\alpha}{\mathrm{d}t} = \sum_{j\in U} m_j\left(\frac{\boldsymbol{\sigma}_i^{\alpha\beta}}{\rho_i^2} + \frac{\boldsymbol{\sigma}_j^{\alpha\beta}}{\rho_j^2} + \boldsymbol{\Pi}_{ij} - \boldsymbol{T}_{ij}\right)\frac{\partial W_{ij}}{\partial \boldsymbol{x}_i^\alpha} + \sum_{j\in\mathfrak{R}} m_j\left(\frac{\boldsymbol{\sigma}_i^{\alpha\beta}}{\rho_i^2} + \frac{\boldsymbol{\sigma}_j^{\alpha\beta}}{\rho_j^2} + \boldsymbol{\Pi}_{ij} - \boldsymbol{T}_{ij}\right)\frac{\partial \mathfrak{R}_{ij}}{\partial \boldsymbol{x}_i^\alpha} + \frac{\boldsymbol{f}_i^\alpha}{m_i}, \\ \frac{\mathrm{d}\boldsymbol{x}_i^\alpha}{\mathrm{d}t} = \boldsymbol{v}_i^\alpha \end{cases} \tag{8}$$

where $\mathfrak{R}_{ij}$ and $\partial\mathfrak{R}_{ij}$ denote kernel function and its gradient of damaged particles, respectively. U and $\mathfrak{R}$ denote the intact and damaged particle ensembles, respectively.

After cracking, a contact strategy following the Newton's second law is proposed to realize the contact behavior (i.e., frictional sliding and topping failure) of rock block along fracture surface. The damaged SPH particles are transformed to discontinuous particles (DPs). The contact behavior of intact particle (IP) and DP is active once the penetration of influence domain U^n of the particle $U^\mathrm{n} > 0$, $U^\mathrm{n} = \frac{R_i+R_j}{2} - d_{ij}$. The contact threshold is determined by the relative spatial position of the two particles, and the contact force is composed with shear contact force $\boldsymbol{F}_i^\mathrm{cs}$ and normal contact force $\boldsymbol{F}_i^\mathrm{cn}$, and is expressed as following:

$$\boldsymbol{F}_i^\mathrm{c} = \boldsymbol{F}_i^\mathrm{cn} + \boldsymbol{F}_i^\mathrm{cs}, \tag{9}$$

where $\boldsymbol{F}_i^\mathrm{cn}$ is determined by the normal stiffness k_n and penetration U^n of the particle influence domain, as follows:

$$\boldsymbol{F}_i^\mathrm{cn} = k_n U^\mathrm{n}\boldsymbol{n}, \tag{10}$$

$$\Delta U^\mathrm{s} = \Delta\boldsymbol{v}_i - \Delta\boldsymbol{v}_i\cdot\boldsymbol{n}, \tag{11}$$

where $\boldsymbol{n}$ represents the unit vector in the direction normal to the relative velocity compared to the previous time step $\Delta\boldsymbol{v}_i$. Then $\boldsymbol{F}_i^\mathrm{cs}$ is determined by the shear stiffness k_s and relative velocity between two particles ΔU^s. It can be defined by

$$\boldsymbol{F}_i^\mathrm{cs} = \left\{\boldsymbol{F}_i^\mathrm{cs}\right\}_\mathrm{update} + k_s\Delta U^\mathrm{s}, \tag{12}$$

$$\bar{\boldsymbol{F}}_i^\mathrm{cs} = \begin{cases} u^\mathrm{f}\boldsymbol{F}_i^\mathrm{cn}\frac{\boldsymbol{F}_i^\mathrm{cs}}{\bar{\boldsymbol{F}}_i^\mathrm{cs}} & \boldsymbol{F}_i^\mathrm{cs} \geq u^\mathrm{f}\boldsymbol{F}_i^\mathrm{cn} \\ \boldsymbol{F}_i^\mathrm{cs} & \boldsymbol{F}_i^\mathrm{cs} < u^\mathrm{f}\boldsymbol{F}_i^\mathrm{cn} \end{cases}, \tag{13}$$

where u^f is the frictional coefficient between the two contact surfaces. Based on coupling the cracking and contact, the governing equation of rock is rewritten as follows:

$$\begin{cases} \frac{\mathrm{d}\rho_i}{\mathrm{d}t} = \sum_{j\in U} m_j\boldsymbol{v}_{ij}\frac{\partial W_{ij}}{\partial \boldsymbol{x}_i^\alpha} \\ \frac{\mathrm{d}\boldsymbol{v}_i^\alpha}{\mathrm{d}t} = \sum_{j\in U} m_j\left(\frac{\boldsymbol{\sigma}_i^{\alpha\beta}}{\rho_i^2} + \frac{\boldsymbol{\sigma}_j^{\alpha\beta}}{\rho_j^2} + \boldsymbol{\Pi}_{ij} - \boldsymbol{T}_{ij}\right)\frac{\partial W_{ij}}{\partial \boldsymbol{x}_i^\alpha} + \frac{\boldsymbol{F}_i^\mathrm{cn}}{m_i} + \frac{\overline{\boldsymbol{F}_i^\mathrm{cs}}}{m_i} + \frac{\boldsymbol{f}_i^\alpha}{m_i}, \\ \frac{\mathrm{d}\boldsymbol{x}_i^\alpha}{\mathrm{d}t} = \boldsymbol{v}_i^\alpha \end{cases} \tag{14}$$

$$\begin{cases} \frac{\mathrm{d}\rho_d}{\mathrm{d}t} = 0 \\ \frac{\mathrm{d}\boldsymbol{v}_d^\alpha}{\mathrm{d}t} = \frac{\boldsymbol{F}_i^\mathrm{cn}}{m_d} + \frac{\overline{\boldsymbol{F}_i^\mathrm{cs}}}{m_d} + \frac{\boldsymbol{f}_d^\alpha}{m_d}. \\ \frac{\mathrm{d}\boldsymbol{x}_d^\alpha}{\mathrm{d}t} = \boldsymbol{v}_d^\alpha \end{cases} \tag{15}$$

Due to the equal and opposite interactions between IPs and DPs based on Newton's third law, as well as the simultaneous transformation of IP into DP upon band loss, the total mass and momentum of the system remain unchanged according to Eqs. (14) and (15).

2.3 Fluid-solid interactions strategy

The fluid–solid interactions are calculated based on an adaptive adjacent integral coupling algorithm considering both the DPs and IPs in Fig. 2. The fluid particles within the influence domain in the solid particles impose the interaction forces on the solid particles, which are mainly contributed by the pressure of the surrounding fluid particles. Therefore, the interaction force $\boldsymbol{f}_\mathrm{F}^\mathrm{S}$ exerted on the solid particle due to the neighbouring fluid particles and interaction force $\boldsymbol{f}_\mathrm{S}^\mathrm{F}$ exerted on the fluid particle due to the neighbouring solid particles.

$$\boldsymbol{f}_\mathrm{S}^\mathrm{F} = -m_\mathrm{S}\sum\nolimits_\mathrm{F} m_\mathrm{F}\left(\frac{P_\mathrm{S}}{\rho_\mathrm{S}^2} + \frac{P_\mathrm{F}}{\rho_\mathrm{F}^2} + \boldsymbol{\Pi}_\mathrm{SF}\right)\nabla_\mathrm{S}W(\boldsymbol{x}_\mathrm{SF}), \tag{16}$$

$$\boldsymbol{f}_\mathrm{F}^\mathrm{S} = -m_\mathrm{F}\sum\nolimits_\mathrm{S} m_\mathrm{S}\left(\frac{P_\mathrm{F}}{\rho_\mathrm{F}^2} + \frac{P_\mathrm{S}}{\rho_\mathrm{S}^2} + \boldsymbol{\Pi}_\mathrm{FS}\right)\nabla_\mathrm{F}W(\boldsymbol{x}_\mathrm{FS}). \tag{17}$$

However, the rock domain consists of IPs and DPs in this study due to cracking. The conventional SPH method lacks an appropriate FSI framework to reproduce the interactions of DPs and fluid particles. The interactions of DPs and fluid should be considered and DP can be regarded as a repulsive particle (Sheikh et al., 2021) for SPH fluid particles referring to the DEM–SPH coupling treatment (W. Xu et al., 2021). Therefore, the interaction forces $\boldsymbol{f}_\mathrm{d}^\mathrm{F}$ and $\boldsymbol{f}_\mathrm{F}^\mathrm{d}$ are treated as the external force (i.e., pressure), which are an equal and opposite reaction from the

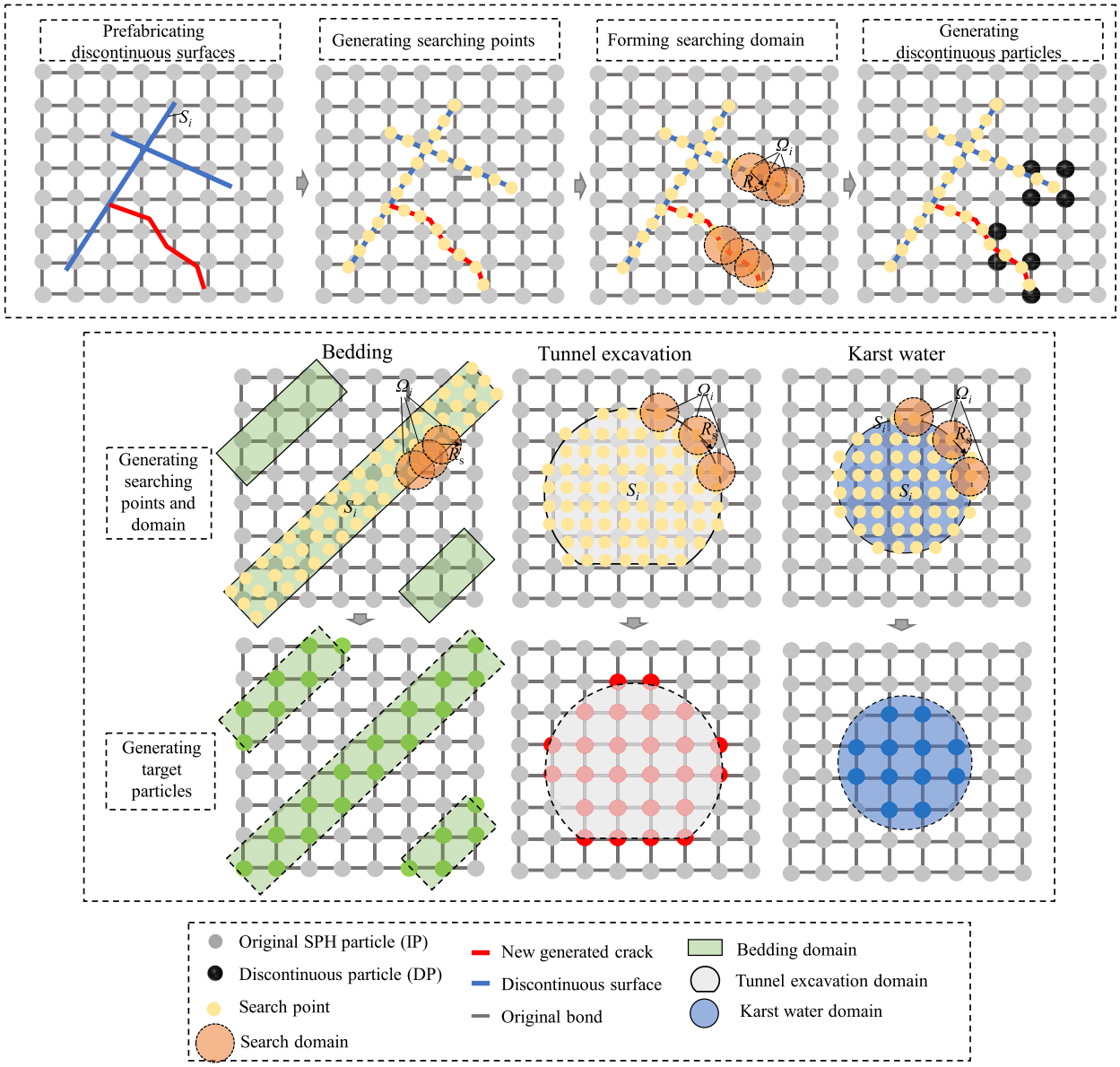

Fig. 2. Schematic view of particle domain searching algorithm.

interacting discontinuous particle d and water particle a due to Newton's third law, and are described using the following formula:

$$\boldsymbol{f}_{\mathrm{F}}^{\mathrm{d}} = -\boldsymbol{f}_{\mathrm{d}}^{\mathrm{F}} = \begin{cases} \chi\left[(r_0/r_{ad})^{12} - (r_0/r_{ad})^{4}\right]\left(\frac{\boldsymbol{x}_{ad}}{r_{ad}}\right), & \text{if } r_0/r_{ad} < 1 \\ 0, & \text{if } r_0/r_{ad} \geq 1 \end{cases}, \tag{18}$$

where $\boldsymbol{f}_{\mathrm{F}}^{\mathrm{d}}$ denotes the interaction force from fluid to DP; $\boldsymbol{f}_{\mathrm{d}}^{\mathrm{F}}$ denotes the interaction force from DP to fluid particles. In general, the cutoff radius r_0 is commonly set to be consistent with the initial particle spacing ΔP according to Monaghan (2005), r_{ad} is distance between the water particle a and discontinuous d. χ is a constant coefficient typically within the same order of magnitude as the square of particle velocity. Therefore, the final momentum equations for FSI considering the DPs and IPs are rewritten as

$$\begin{cases} \frac{\mathrm{d}\boldsymbol{v}_i^{\alpha}}{\mathrm{d}t} = \sum_{j\in U} m_j\left(\frac{\boldsymbol{\sigma}_i^{\alpha\beta}}{\rho_i^2} + \frac{\boldsymbol{\sigma}_j^{\alpha\beta}}{\rho_j^2} + \boldsymbol{\Pi}_{ij} - \boldsymbol{T}_{ij}\right)\frac{\partial W_{ij}}{\partial \boldsymbol{x}_i^{\alpha}} + \frac{\boldsymbol{f}_i^{\alpha}}{m_i} + \frac{\boldsymbol{F}_i^{\mathrm{cn}}}{m_i} + \frac{\overline{\boldsymbol{F}_i^{\mathrm{cs}}}}{m_i} - \boldsymbol{f}_{\mathrm{S}}^{\mathrm{F}} \\ \frac{\mathrm{d}\boldsymbol{v}_a^{\alpha}}{\mathrm{d}t} = \sum_{b=1}^{N} m_b\left(\frac{P_a}{\rho_a^2} + \frac{P_b}{\rho_b^2} + \boldsymbol{\Pi}_{ab}\right)\frac{\partial W_{ab}}{\partial \boldsymbol{x}_a^{\alpha}} + \frac{\boldsymbol{f}_a^{\alpha}}{m_a} - \boldsymbol{f}_{\mathrm{F}}^{\mathrm{S}} + \boldsymbol{f}_{\mathrm{F}}^{\mathrm{d}} \\ \frac{\mathrm{d}\boldsymbol{v}_d^{\alpha}}{\mathrm{d}t} = \frac{\boldsymbol{f}_d^{\alpha}}{m_d} + \frac{\boldsymbol{F}_d^{\mathrm{cn}}}{m_d} + \frac{\overline{\boldsymbol{F}_d^{\mathrm{cs}}}}{m_d} + \boldsymbol{f}_{\mathrm{d}}^{\mathrm{F}} \end{cases}, \tag{19}$$

where $\frac{\mathrm{d}\boldsymbol{v}_i^{\alpha}}{\mathrm{d}t}$, $\frac{\mathrm{d}\boldsymbol{v}_a^{\alpha}}{\mathrm{d}t}$, and $\frac{\mathrm{d}\boldsymbol{v}_d^{\alpha}}{\mathrm{d}t}$ denote the momentum of IP, fluid particle and DP, respectively. $\boldsymbol{f}_i^{\alpha}$, $\boldsymbol{f}_a^{\alpha}$, and $\boldsymbol{f}_d^{\alpha}$ are external force of IP, fluid particle, and DP, respectively.

2.4 Explicit particle search method

The explicit particle search (EPS) method (Fig. 2) is introduced to generate the muti-phase domain (i.e., solid and fluid phase), discontinuous surface (i.e., detect, joint, bedding plane and fault) and crack propagation at any

angle without the need to refine the mesh in these particle domains. By distributing searching particles evenly in the generated contours and assigning a searching radius to each particle, this algorithm can accurately locate the particles to be transformed, ensuring that they are located inside the muti-phase domain and discontinuous surfaces or cracks. The process is detailed as follows: Firstly, the arbitrary discontinuous surfaces S_i ($i = 1, 2, \cdots, n$) (indicated by blue in Fig. 2) are prefabricated in the rock-like matrix domain. Then the searching points M_i with searching radius R_s, which is equal to the value of smoothing kernel radius h, are located uniformly on each discontinuous surface S_i. Once the original particles (IPs) are covered by the searching domain Ω_i formed by searching radius R_s, the IPs in Ω_i are defined as the DPs or deleted. The searching treatment of newly generated cracks is similar to the one of discontinuous surfaces.

Furthermore, the generation of the multi-phase domain, including the weak bedding and tunnel excavation surfaces and karst water domain, is accomplished through a systematic process of searching particles within a specified searching radius R_s. Each target IP within the search domain Ω_i is assigned distinct material parameters based on their respective roles, with specific attributes assigned to weak bedding planes and water bodies. As part of this process, IPs situated on the tunnel excavation surface are promptly removed from the simulation to accurately represent the tunnel opening. Therefore, the EPS method can greatly reduce the computational cost to model the complex muti-phase domains (i.e., solid and fluid phase), discontinuous surfaces (i.e., detect, joint, bedding plane and fault), and crack propagation.

3 Benchmark test

The water/mud inrush phenomenon in rock tunnels involves intricate failure and FSI processes, encompassing rock fracturing, inrush flow, interactions of water–rock, and the contact behavior of rock blocks. To validate the effectiveness of the CDSPH method, two FSI laboratory tests are conducted. The first involves a well-established hydraulic fracturing test utilized to verify the FSI and hydraulic fracturing. The second test comprises a flume experiment on sliding-induced impulsive waves, aiming to authenticate the FSI and contact behavior of the SPH rock model.

3.1 Hydraulic fracturing test

To validate FSI and crack behavior in the CDSPH rock model, rock samples with specific flaw water pressures from Mu et al. (2022) were chosen for numerical simulations. Figure 3 illustrates a rock sample featuring two parallel prefabricated flaws, measuring 76.2 mm in length and 152.4 mm in width, consisting of 18 000 particles. The prefabricated flaws have an dip angle $\beta^{ang} = 45°$, and the angle $\alpha^{ang} = 45°$ is formed between the connecting line of the inner tips of the flaws and the extension line of flaw 2. The initial particle spacing at $\Delta P = 0.8$ mm corresponds to a smoothing kernel radius of $h = 0.7$ mm, aimed at preventing SPH kernel interaction between the IPs flanking the DPs (Chakraborty et al., 2017). In addition, the loading rate imposed on the upper and bottom boundary particles was 0.5 m/s, and the time step of the calculation was $\Delta t = 5 \times 10^{-8}$ s. For detailed boundary particle configurations and parameter, refer to Zhou et al. (2015a). In this section, the influence of different inclination angles ($\theta = 0°$, 30°, 45°, 60°, 90°) of weak layer on the hydraulic fracturing behavior of the rock model was thoroughly investigated. The weak layer materials parameters are adopted from Xu et al. (2017). To address rock heterogeneity, a Weibull distribution with a shape parameter m^h of 20 (Zhou et al., 2015b) was employed. Table 1 illustrates the SPH parameters for the stratified rock sample featuring two parallel prefabricated flaws.

In Fig. 4, the crack distributions and stress–strain curves (SSC) of SPH models of intact are directly compared. The results reveal that apparent elastic modulus (6.12 GPa) and uniaxial compressive strength (UCS) (17.6 MPa) obtained from the stress–strain curve of the CDSPH model (intact) are highly consistent with the results of Total Lagrangian SPH (TLSPH) (intact) (Mu et al., 2022) and the difference is within 1%. Moreover, the crack distributions and failure modes of double cracks are highly consistent with those obtained by the TLSPH method and experiment (Bi & Zhou, 2017). The result proves the accuracy and feasibility of the CDSPH method for simulating fracture and FSI processes.

Sensitive analysis of different θ on cracking patterns and SSC of SPH are directly shown in Fig. 5 and Fig. 4(c). Pressure is continuously applied in both the bore hole and the newly formed fracture surfaces as the fractures propagate. It is considered that when a particle is fully damaged and/or the aperture is large enough, the water particles can flow inside the fracture and the hydraulic pressure is applied on the fracture surfaces (Douillet-Grellier et al., 2016). The results reveal that the particle spacing significantly affects the final cracking pattern, particularly in relation to the expansion of wing cracks induced by hydraulic pressure, quasi-planar shear cracks, and tensile coalescence cracks. Furthermore, the presence of weak bedding planes moderately reduces UCS, and the UCS exhibits a U-shaped distribution with bedding dip angle θ increasing. At $\theta = 60°$, the UCS reaches its minimum value (7.29 MPa), representing only 41% of the intact rock strength (17.6 MPa). Conversely, at $\theta = 90°$, the UCS reaches its minimum value (17.2 MPa), accounting for 97% of the intact rock strength. Therefore, comprehensively considering the characteristics of bedding planes is essential when simulating tunnelling processes involving water and mud in the presence of bedding planes. Their influence on the cracking pattern and UCS should not be underestimated. Adequate consideration of bedding plane properties will lead to more accurate and reliable simulation results, pro-

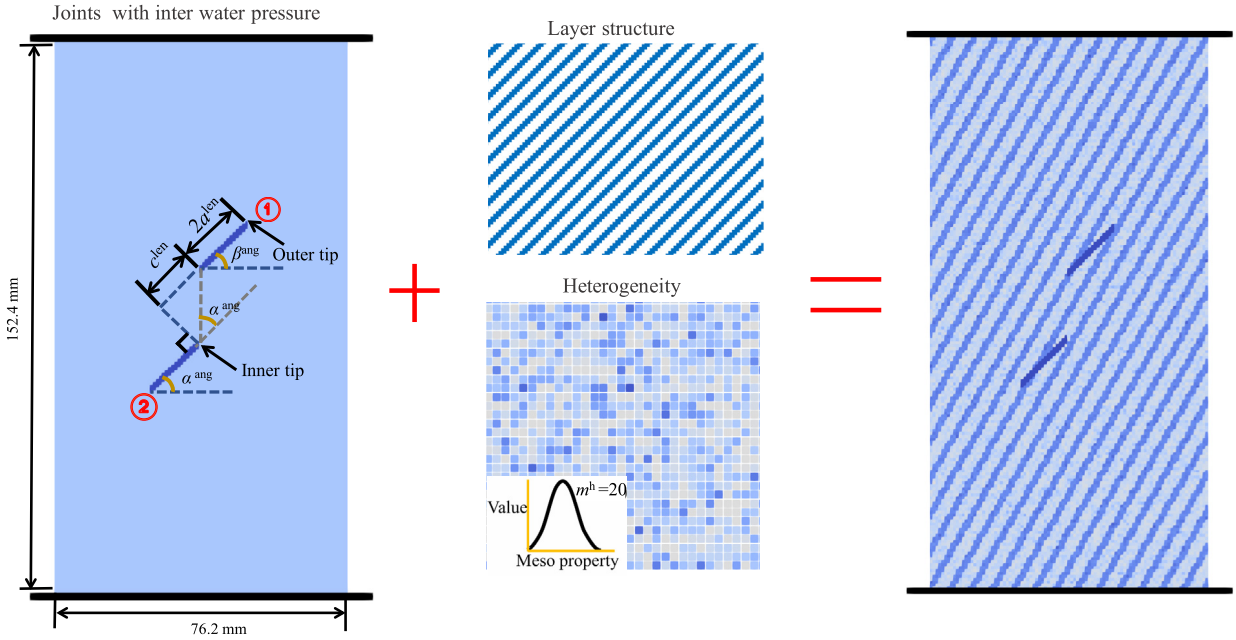

Fig. 3. Model configuration of the unconfined compression tests considering the layer structure and heterogeneity (c^{len} and a^{len} represent the crack length and the length of the rock bridge parallel to the crack extension direction, respectively).

Table 1
CDSPH parameters of the sample with two parallel prefabricated flaws.

Parameters	Rock matrix	Water	Bedding plane
Density (kg/m^3)	2650	1000	2650
Elastic modulus (GPa)	6	–	6
Internal friction angle (°)	45	–	35
Cohesion (MPa)	50	–	24
Poisson's ratio	0.28	–	0.28
Tensile strength (MPa)	23	–	11
Friction coefficient	tan (35°)	–	tan (22°)
Normal stiffness (GPa/m)	0.2	–	0.2
Particle spacing (m)	8×10^{-3}	8×10^{-3}	8×10^{-3}
Number of IPs	11 966	50	5984
Kernel function	Cubic	Cubic	Cubic
Kernel smoothing length (m)	7×10^{-3}	7×10^{-3}	7×10^{-3}
DP radius (m)	8×10^{-3}	–	8×10^{-3}
SPH time step (s)	5×10^{-8}	5×10^{-8}	5×10^{-8}
δ-SPH coefficient	–	0.1	–
Shape parameter	20	–	20
Controlling parameter β_1 for artificial viscosity	1	1	1
Controlling parameter β_2 for artificial viscosity	2	–	2
Parameters e_1 for artificial stress	0.3	6.0	0.3
Parameters e_2 for artificial stress	4	–	4

viding valuable insights for dealing with tunnelling under challenging geological conditions.

3.2 Flume experiment of sliding induced impulsive wave

The correctness of the contact and FSI is verified by laboratory flume experiments. The flume experimental test of sliding induced impulsive wave was carried out in a transparent acrylic plate square tank as shown in Fig. 6(a). One side of the acrylic plate was covered with lattice paper, and the other side was installed with a high-speed camera to capture the process of the block sliding into the water, generate pulse waves, and determine the height and position of the guided wave. It is used to verify the correctness of the FSI in CDSPH. The length of the test tank is 1 m, and the depth is 0.5 m. The bottom of the tank is semicir-

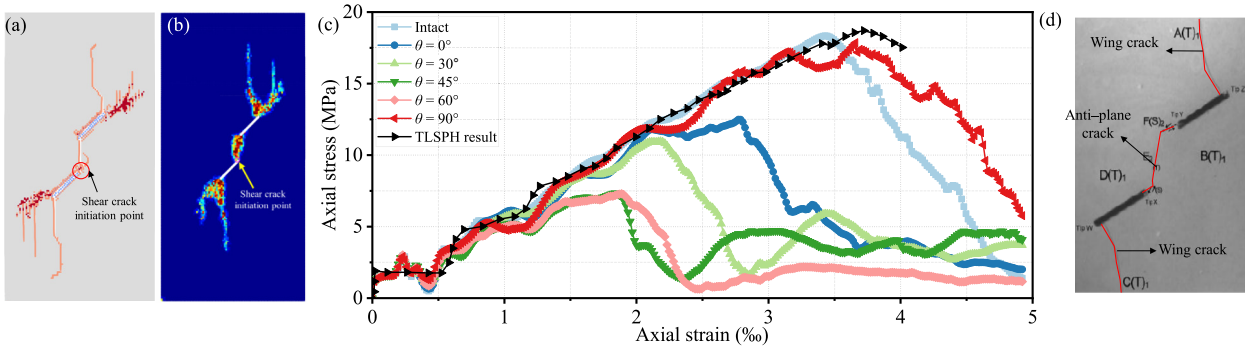

Fig. 4. (a) Crack distribution of the rock sample calculated by CDSPH (The orange and red colours represent tensile and shear cracks in the CDSPH results, respectively.) and compared with (b) TLSPH result (Mu et al., 2022), (c) stress-stain data curves of the rock sample with different dip angles θ, and (d) crack distribution of rock sample obtained from experiment (Bi & Zhou, 2017).

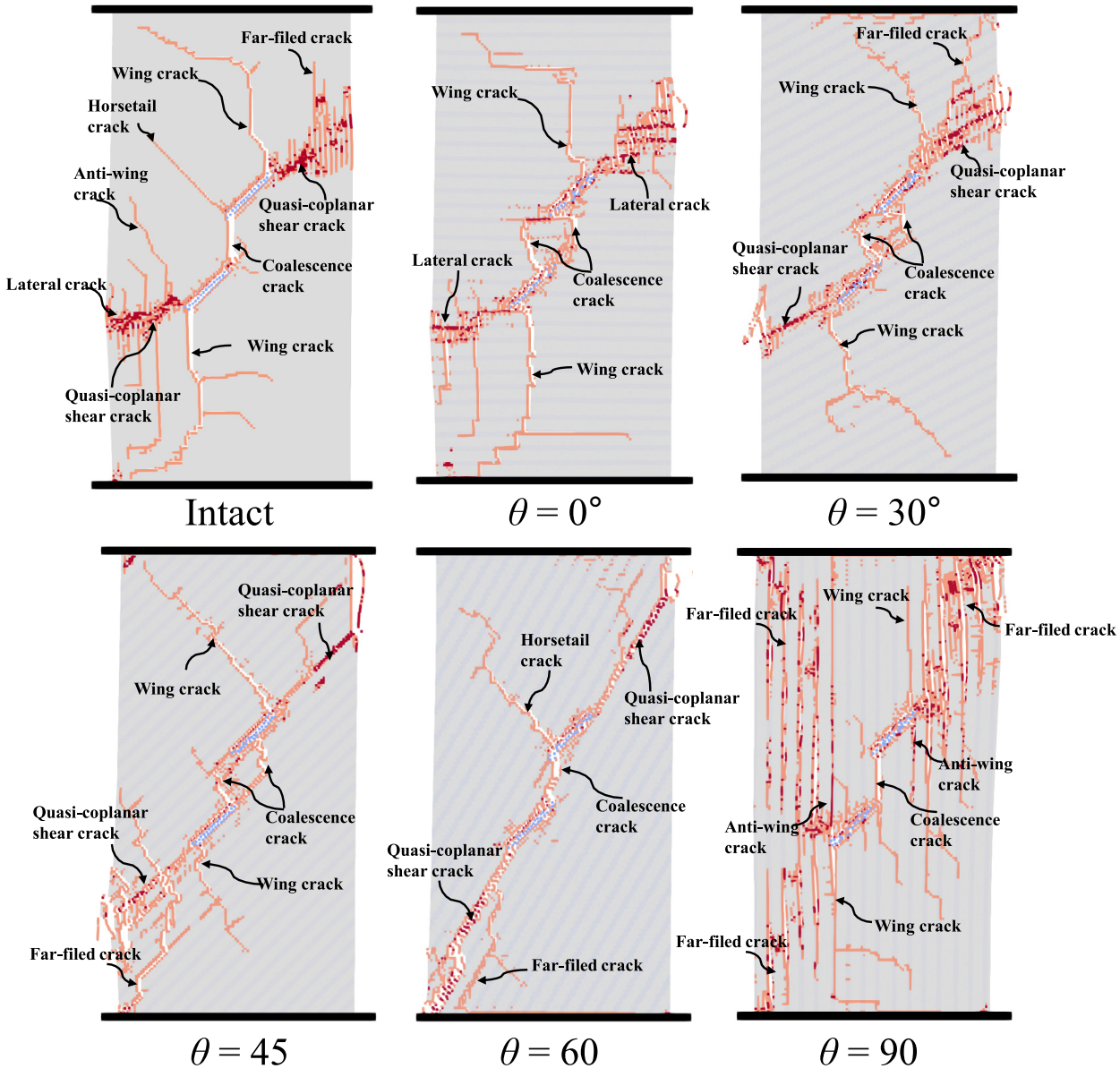

Fig. 5. Final Crack distribution of the rock sample with two parallel prefabricated flaws under normal loading ($\alpha = 45°$, $\beta = 30°$) with different dip angles θ.

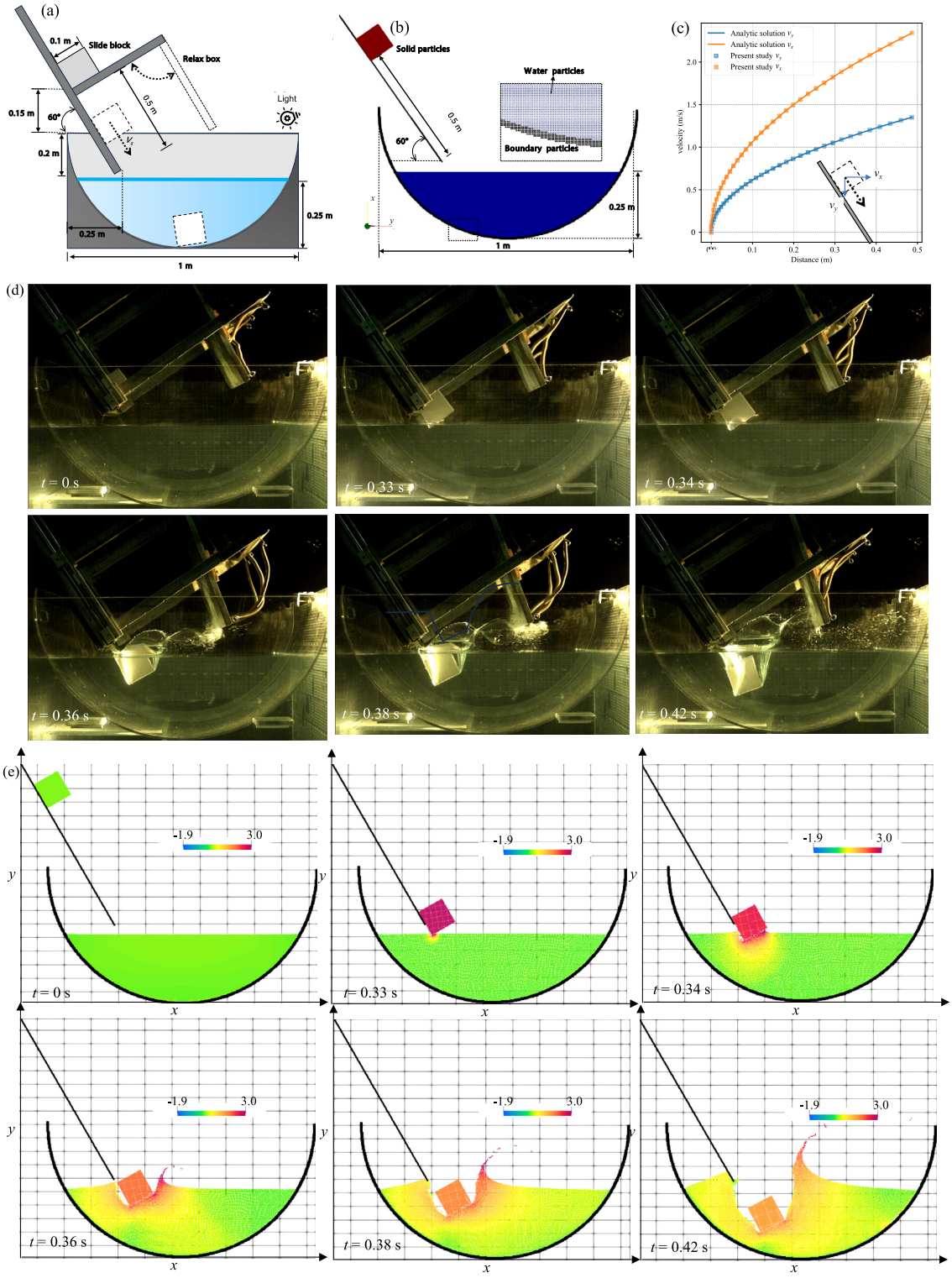

Fig. 6. (a) Model configuration and (b) CDSPH model of sliding induced impulsive wave, (c) horizontal and vertical velocity with total distance with $\mu^{fric} = 0.2$, compression of free surface flow and velocity field (m/s) of the block and water at different moments between (d) experiment and (e) simulation result.

cle, the radius is 0.5 m, and the experimental fluid is water, and the depth is 0.25 m. The material of the square block is gypsum with a density of about 1850 kg/m^3. The temperature of the sliding block is controlled at about 25 °C. Friction coefficient μ^{fric} between the sliding surface and the sliding block is 0.2, while the friction coefficient between

the sliding surface and the semicircular tank is approximately 0. The dip angle of the sliding plate is $\lambda = 60°$. Sliding body is about 0.45 m higher than the water surface, and the release of the sliding block is controlled by the electrokinetic gate. When the gate is released, the sliding body slides into the water body along the sliding surface under the action of gravity, surging waves in tank. Meanwhile, the corresponding CDSPH model is established as shown in Fig. 6(b). Square sliding block consisting of IPs with a side length of 1 m was simulated sliding freely on a straight surface composed of DPs with dip angle of 60° under the influence of gravity. The specific parameters of the SPH particles are provided in Table 2. The sliding block was uniformly discretized with initial particle spacing of $\Delta P = 2.5 \times 10^{-4}$ m, where $\boldsymbol{g} = 9.81$ m/s^2 represented the acceleration due to gravity, and t denoted the sliding time of the block. The SPH time step is set as 5×10^{-6} s.

Initially, Fig. 6(c) illustrates the velocity evolution of the square sliding block at sliding plate. The sliding force is greater than the maximum static friction force, and the velocity of the block can be obtained by the analytical solution according to the Coulomb friction contact theory (Zhan et al., 2020). Importantly, the CDSPH numerical results exhibit excellent agreement with the analytical solution. This straightforward benchmark test confirms that the CDSPH method precisely simulates the frictional sliding behavior of fractures, constituting a critical step towards reliable modeling of large deformations and contacts in rock masses within karst tunnels.

Subsequently, the interaction between the sliding body and the fluid after immersion is examined in Fig. 6(e). The CDSPH method reflected the free surface flow of the fluid and its impact on the sliding block in Fig. 6(f). Specifically, it accurately represented the presence of voids before and after the object. Monitoring the water tongue height and its horizontal position via high-speed cameras revealed values close to the CDSPH simulation, with errors of 2.3% and 3.8%, respectively. The simulated fluctuations of the free surface were higher than those observed in the experiments, primarily due to the two-dimensional nature of the simulation, preventing the spreading of water to the surrounding interface and resulting in a notable elevation of the two-dimensional water surface compared to the three-dimensional actual scenario.

Table 2
Parameters of CDSPH particles in sliding induced impulsive wave test.

Parameters	Block	Water
Density (kg/m^3)	1850	1000
Elastic modulus (GPa)	0.01	–
Poisson's ratio	0.3	–
Normal stiffness (MPa/m)	9.6	–
Friction coefficient of slide plate	0.2	–
Friction coefficient of water tank	0	–
Particle spacing (m)	2.5×10^{-4}	2.5×10^{-4}
Boundary particle spacing (m)	0.2	0.2
Number of particles	1512	14 250
Kernel function	Cubic	Cubic
Kernel smoothing length (m)	2.5×10^{-4}	2.5×10^{-4}
DP radius (m)	2.5×10^{-4}	–
SPH time step (s)	5×10^{-6}	5×10^{-6}
Controlling parameter β_1 for artificial viscosity	1	1
Controlling parameter β_2 for artificial viscosity	2	2
Parameters e_1 for artificial stress	0.3	–
Parameters e_2 for artificial stress	4	–
δ-SPH coefficient	–	0.1

4 Numerical simulation of the QYS tunnel

The stratified karst tunnel involves processes related to rock damage, contact, and FSI. The validity of CDSPH method in realizing rock damage, contact, and FSI is verified by two experiments. Therefore, we applied CDSPH methods to a QYS karst tunnel to comprehensively investigate its progressive failure and hazards associated with sudden water/mud inflow considering different dip angles (θ) and karst cave positions.

Passive techniques are employed here to address issue of fluid particles penetrating solid particles. Firstly, a level of interaction force is introduced between fluid and solid particles to prevent mutual penetration. Secondly, stability within the computational domain is maintained through the implementation of the XSPH algorithm (Monaghan, 2005), regulating particle velocities. Lastly, the reduction of the time step helps to prevent the mutual penetration of fluid and solid particles.

4.1 Engineering background

The QYS karst tunnel, with a total investigated length of 10.528 km in Hubei Province, China, spans from ZK19 +005 to ZK22+380 and has a maximum burial depth of approximately 0.67 km (Z. Xu et al., 2021). The tunnel traverses a stratum comprising medium-thick limestone with shale and coal seams, which is marked by layering and is a typical strong karst aquifer (Fig. 7(a)). As a result, the tunnel is surrounded by numerous highly water-rich karst caves, which are often fed by surface water from the surrounding QYS area. This has caused severe sudden water and mud inflow disasters during heavy rains, such as the maximum water inflow of 1.153×10^4 m^3/h observed at ZK19 + 750 to ZK20 + 150 and YK19 + 740 to YK20 + 155 during the rainy season of 2015, with high water pressure and stress concentration caused by the presence of karst caves being the primary causes of such disasters.

4.2 Computation model and parameters

A 2D numerical model with a 70 m height and 70 m width was established to investigate the mechanical behavior of a tunnel under the influence of a single karst cave based on FSI, as depicted in Fig. 7(b), based on field investigation and prior research (Z. Xu et al., 2021). The EPS method was employed to simulate the generation of bed-

ding planes, tunnel excavation, and karst water in the numerical model. In this model, the karst cavity with a high-pressure model was simplified. The radius of the karst cave on the tunnel face was 6 m and the initial water pressure of the karst cavity adjacent to the tunnel was 0.12 MPa. The tunnel face was approximately 9 m in

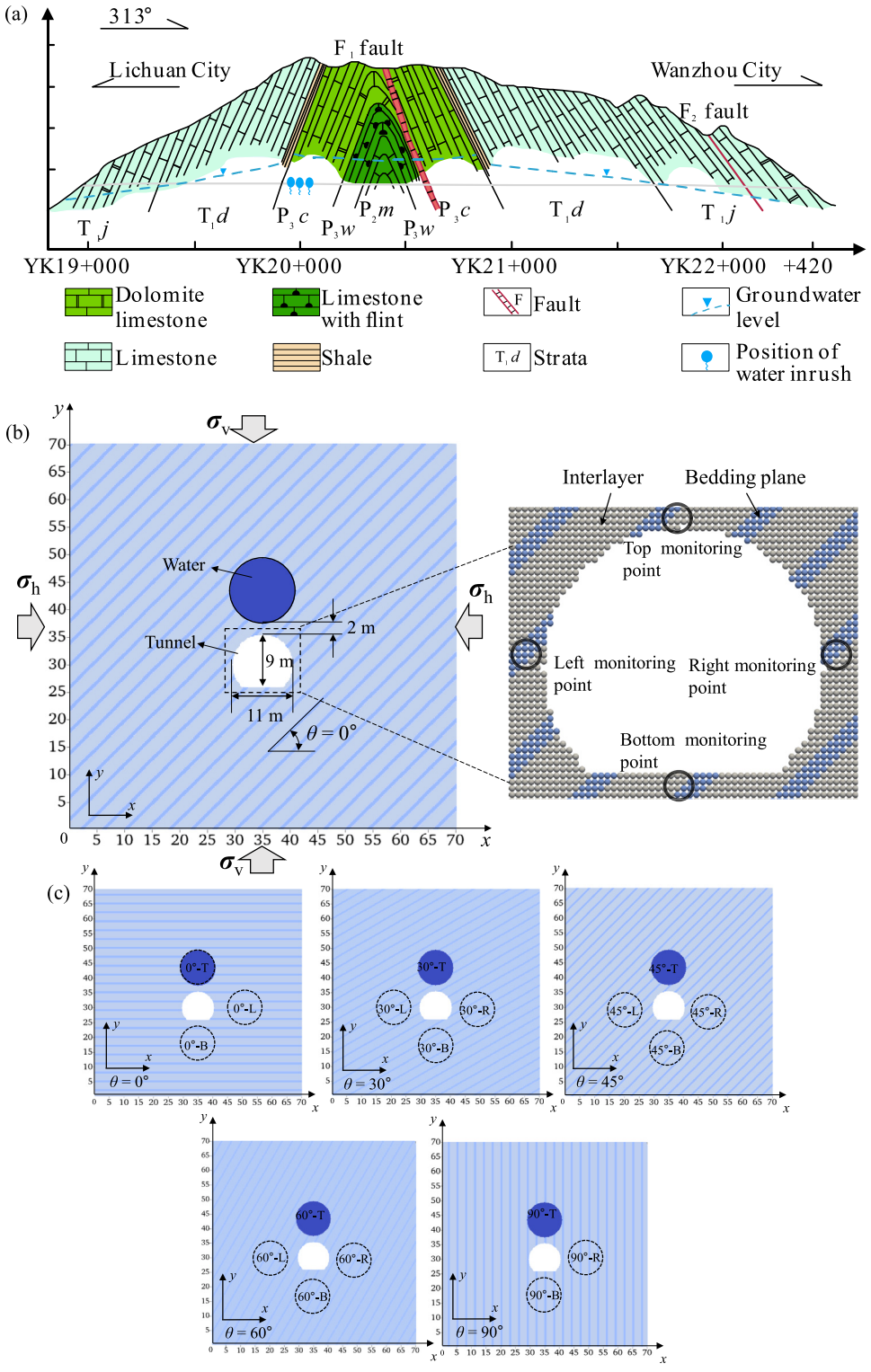

Fig. 7. (a) Longitudinal geological section along the Qiyueshan tunnel (after Gao et al. (2021)), (b) model configuration and base particle, and (c) different scenarios of karst cave.

Table 3
Parameters of SPH particles used in QYS karst tunnel.

Parameter	Rock matrix	Bedding plane	Water
Density (kg/m^3)	2500	2500	1000
Elastic modulus (GPa)	12	4	–
Poisson's ratio	0.25	0.35	–
Cohesion (MPa)	50	30	–
Tensile strength (MPa)	30	20	–
Internal friction angle φ (°)	30	25	–
Normal stiffness (MPa/m)	9.6	3.2	–
Friction coefficient	tan 30°	tan 25°	–
Particle spacing (m)	0.2	0.2	0.2
Boundary particle spacing (m)	0.2	0.2	0.2
Number of particles	60 250	10 250	1512
Kernel function	Cubic	Cubic	Cubic
Kernel smoothing length (m)	0.2	0.2	0.3
DP radius (m)	0.2	0.2	–
SPH time step (s)	1×10^{-4}	1×10^{-4}	1×10^{-4}
δ-SPH coefficient	–	–	0.1
Controlling parameter β_1 for artificial viscosity	1	1	1
Controlling parameter β_2 for artificial viscosity	2	2	2
Parameters e_1 for artificial stress	0.3	0.3	–
Parameters e_2 for artificial stress	4	4	–

height, with a maximum width of 10 m. The karst cave was located approximately 2 m above the top of the tunnel face according to Z. Xu et al. (2021).

The material parameters for rock SPH particles were obtained through a site survey and literature review (Lai et al., 2021; Z. Xu et al., 2021), as shown in Table 3. It is worth noting that the cohesion and tensile strength values require calibration and are greater than the actual values of real-world rocks. The kernel length was set at $h = 0.2$ m to prevent the SPH kernel interaction of the IPs on the two sides of the DPs (Shaw et al., 2015), and the boundary of the model consisted of virtual particles (Bi & Zhou, 2015) to prevent base particles from overflowing the boundary. The real gravity acceleration ($g = 9.8$ m/s^2) was considered to replicate the real flow of water and rock movement after rock collapse and water inrush.

In consideration of the initial ground stress, and following the approach taken by (Z. Xu et al., 2021), the limestone above the model was assumed to be 500 m thick with an average overlying density of 2000 kg/m^3. According to the depth of the tunnel, the weight of the rock and soil above is converted into an equivalent load and added to the upper boundary of the SPH model (Lai et al., 2021). Therefore, a normal vertical pressure $\boldsymbol{\sigma}_v$ of 10 MPa was applied to the vertical boundary of the model by setting a vertical velocity of virtual particles (Shu et al., 2020) while the bottom remained fixed. A lateral pressure $\boldsymbol{\sigma}_h$ of 5 MPa was applied to the lateral side of the tunnel. Once a desired constant stress magnitude was achieved throughout the tunnel, the velocity of the top boundary was stopped. During the balancing process, the infinite shear and tensile strength of the rock mass were imported. When the expected ground stress was achieved, the actual tensile and shear strength were imported, and the calculation time was set as 0 s. The calculation time step was 5×10^{-5} s, and a total of 40 000 steps were calculated in this study.

To ensure that the impact of the single karst cave on the stratified tunnel is thoroughly analyzed, we considered five sets of bedding angles (i.e., 0°, 30°, 45°, 60°, and 90°) and four cave locations (i.e., left, right, roof, and bottom of tunnel), resulting in a total of 18 different scenarios as shown in Fig. 7(c). In addition, the layer spacing of all bedding dips is set as consistent, and the interlayer thickness is controlled to be 3–5 times the bedding thickness. The displacement of the corresponding water-resistant layers at different locations and the stress, as well as the number of cracks formed were monitored, as shown in Fig. 7(b). It should be noted that this 2D numerical model simplifies the actual tunnelling process and does not consider the impact of previous construction disturbance on the stress field, as per the two-band theory proposed by Li et al. (2015). Furthermore, we assumed that the stratified tunnel was only affected by a single water-filled karst cave, and the weakened zone caused by karst water fracturing was studied.

4.3 Calculation results and analysis

Understanding tunnel failure characteristics and accurately predicting the safe relationships between layer dip angles and karst cave positions are essential measures for identifying and mitigating water inrush hazards. Upon reaching the critical threshold of combined bedding dip angles and karst cave positions, prudent measures such as advancing support or other protective mechanisms must be taken in order to avert potential inrush accidents (Gao et al., 2023). It is analytically discerned that varying patterns of the bedding dip angle and the karst cave position significantly influence the failure mode of the tunnel and the risks of water inrush.

In this study, to facilitate the presentation of the failure mode, we have selected and presented the main failure area of the cave (10 m × 20 m). The failure process of the water-resistant rock between the cave and the tunnel was extremely short and rapid, lasting only 1.25 s. Therefore, the precursory behavior of water and mud inrush will be of utmost importance. The CDSPH algorithm, which embeds the Lagrangian method, the contact algorithm and the improved adaptive adjacent integral coupling algorithm, has achieved a progressive failure of the stratified water-resistant rock under high in-situ stress (from crack propagation to contact slip, and even rolling) and the water and mud inrush process of the karst tunnel.

4.3.1 Analysis of roof failure and water inrush

Figure 8 illustrates the progressive roof failure of the water-resistant structure of tunnels with different dip angles

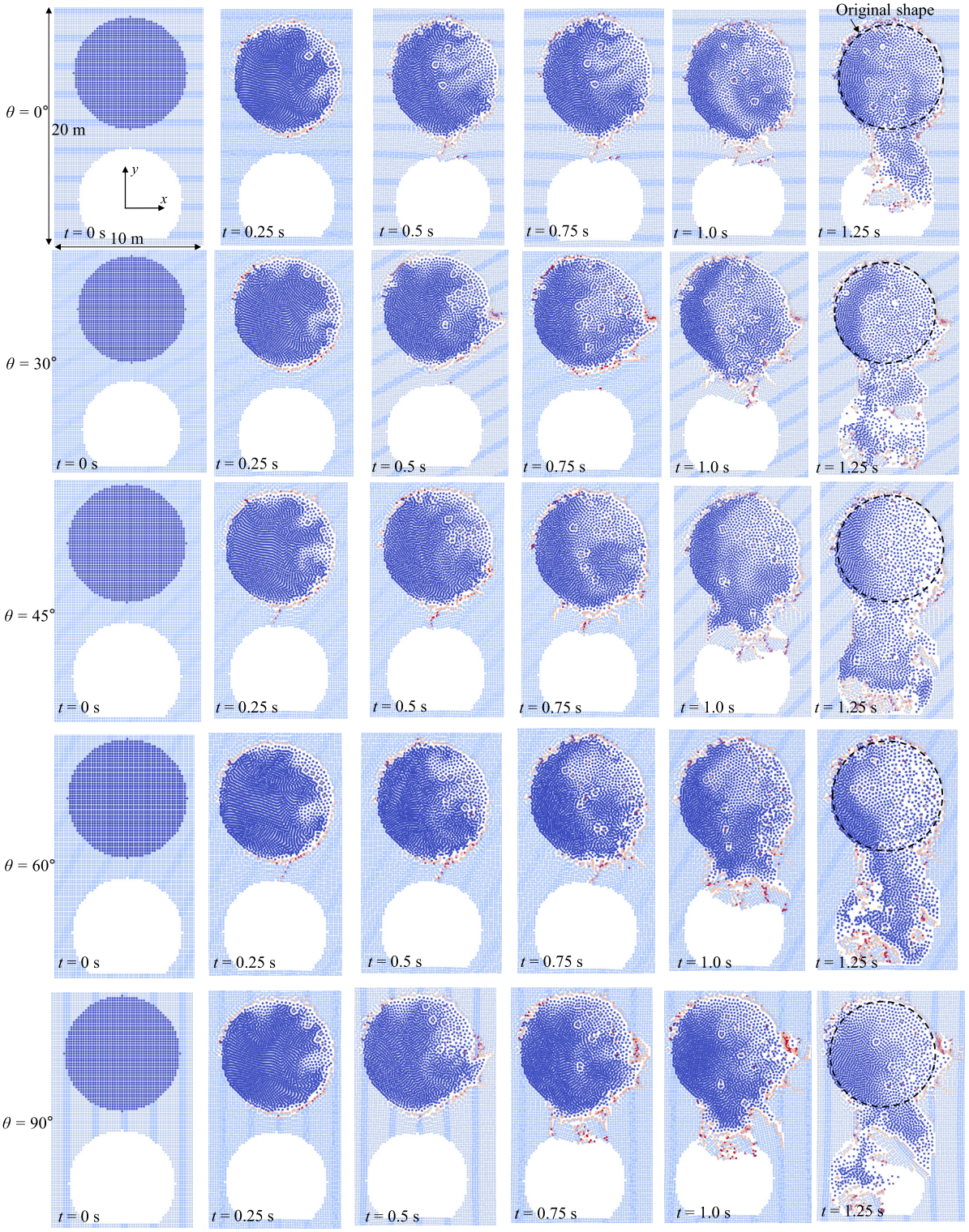

Fig. 8. Entire process of progressive rock damage and water inrush with different θ when karst cave is located at the roof of tunnel.

θ when karst cave is located at the roof of tunnel. Intuitively, it can be observed that the water-resistant rock surrounding the tunnel with different θ experiences varying degrees of damage and water/mud inrush subject to the overlying water pressure and high ground stress. Complete rock fracture and collapse of water-resistant structure with dip angles $\theta = 45°$ and $60°$ are observed at $t = 1.25$ s, and inrush occurs in a fully submerged manner. The reason is that the surrounding rock first forms a dominant fracture surface due to shear cracking before water inrush, which

propagates along the bedding direction with 60° ± ϕ/2 (ϕ denotes internal friction angle) according the Mohr–Coulomb failure criterion with a tension cut-off. Consequently,water inrush in the overlying cave is more possible to occur at θ = 45° and 60°. In addition,the temporary local inrush is observed at θ = 0° and 90° for water-resistant structure.

Moreover, the water in the karst cave continually eroded the cave walls during the rock failure, leading to corresponding changes in the karst cave morphology which is consistent with the field observation. This strongly physical erosion process based on fluid–solid interaction in SPH is difficult to be revealed by other block methods (like Universal Distinct Element Code (UDEC)). Furthermore, the internal sudden water inrush in the karst cave not only acted on the water-resistant rock of invert directly but also caused complete collapse of the sidewalls, such as the right sidewall of θ = 90° at 1.25 s.

For further quantification of the impact of dip angles of stratified rock tunnels on failure characteristics, the vertical stress at the measuring points at the top of the tunnel is depicted in Fig. 9(a). It can be found that the rock cracking and collapse process of the water-resistant structure can be divided into four consecutive stages. At the beginning of the water–rock interaction simulation, the corrosive effect of the water on the karst cave surrounding rock mass causes the vertical stress to be relatively stable at 5 MPa (Stage I). Under the action of overlying water pressure, the surrounding rock enters the elastic strain stage, and the blocks lose resistant capacity after reaching the peak stress successively. Then, a stress drop occurs, and the water-resistant rock fractures until the crack penetrates the water-resistant rock (Stage II). Among them, the water-resistant rocks with θ = 0° and 90° display brittle failure characterized by a rapid drop in stress during the post-failure stage. In contrast, rocks with θ = 30°, 45°, and 60° exhibit ductile failure behavior. During Stage III, which is the block sliding stage, stress rebound is observed in the case with θ = 60°, attributed to multiple frictions between the separating blocks and the surrounding rock. This frictional interaction leads to the occurrence of multiple fractures in the rock mass. After the block separates

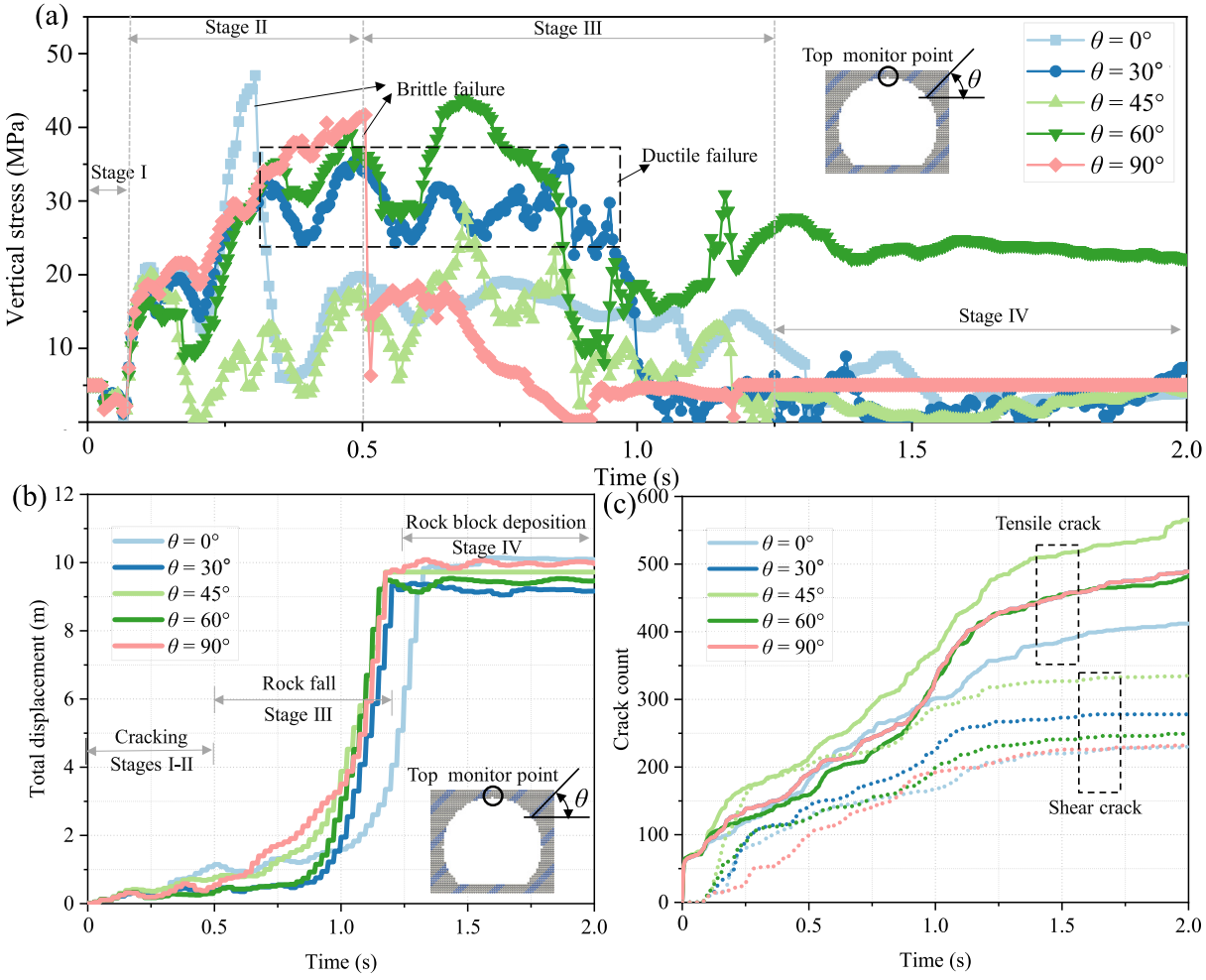

Fig. 9. Evolutions of (a) vertical stress, (b) total displacement, and (c) crack count of stratified tunnel with different θ when karst cave is located at the roof of tunnel.

from the surrounding rock, water rushes in extensively. This stage (Stage IV) is accompanied by the falling of rock blocks from the tunnel roof and their deposition at the tunnel bottom, with stress gradually returning to equilibrium.

By conducting a comparative analysis of peak stresses at different dip angles prior to the stress drop, it was observed that the peak stresses at 0° and 90° were more substantial than those at other angles, reaching 46 and 41 MPa, respec-

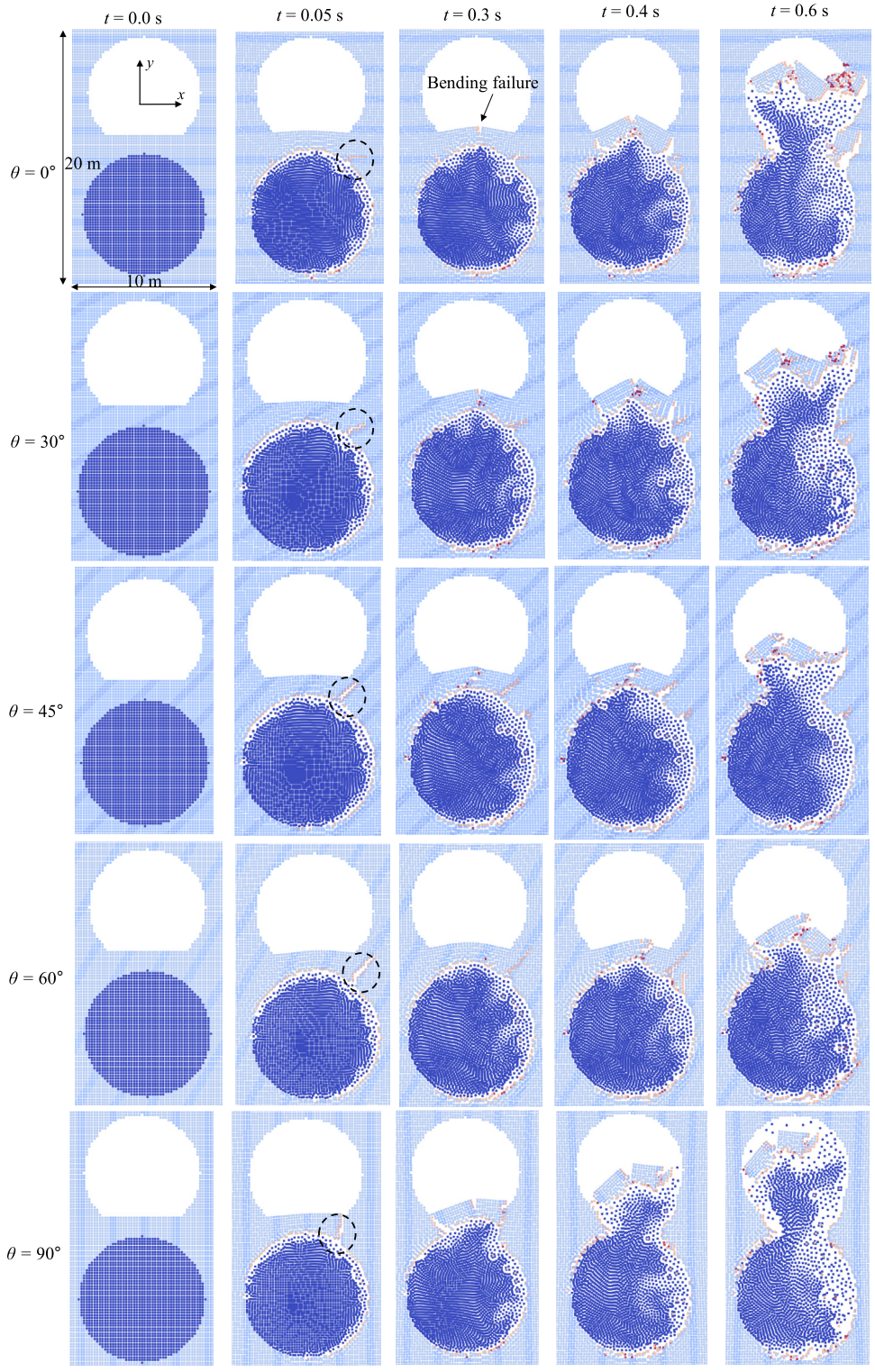

Fig. 10. Entire process of progressive rock damage and water inrush with different θ when karst cave is located at the bottom of tunnel.

tively, and displayed brittle failure characteristics. The peak stress at 30° was comparatively lower at 36 MPa and exhibited ductile failure characteristics. For the case with $\theta = 45°$ and 60°, lying between brittle and ductile behaviors, the peak stresses were relatively smaller, and cracks rapidly propagated during Stage II, resulting in stress escalation during Stage III frictional sliding. Hence, the vertical stress obtained by the CDSPH method can provide a comprehensive understanding of the progressive failure process of the surrounding rock with different dip angles.

Figure 9(b) presents the total displacement of the measuring points. It can be found that the rockfall primarily occurred during the late stage of Stage IV, and for $\theta = 0°$, the falling time was relatively delayed compared to other dip angles, suggesting that horizontal rock layers offer relatively greater stability. The evolution of crack count is depicted in Fig. 9(c). The crack count progressively increases from Stage II to Stage III and then accelerates, eventually reaching a stable state. Importantly, the number of tensile cracks exceeds that of shear cracks, indicating that tensile failure dominates during inrush, which is consistent with the site observstion (Lai et al., 2021; W. Xu et al., 2021). Moreover, the water-resistant structure with $\theta = 45°$ poses the greatest hazard due to highest crack formation, whereas a dip angle of 0° signifies the most stable condition. These findings underscore the critical influence of dip angles on the behavior and failure patterns of water-resistant structures in stratified tunnels, offering valuable insights for engineering safety assessments and mitigation strategies.

4.3.2 Analysis of bottom failure and water inrush

The entire process of progressive rock damage and water inrush at tunnel bottom with different θ is depicted in Fig. 10. The rock damage of the bottom position at $t = 0.3$ s is similar to the bending failure mode in the three-point bending test of slate (An et al., 2021; Fang et al., 2022), and hydraulic fracture starts from the edge of the cave and first expands along the weak plane direc-

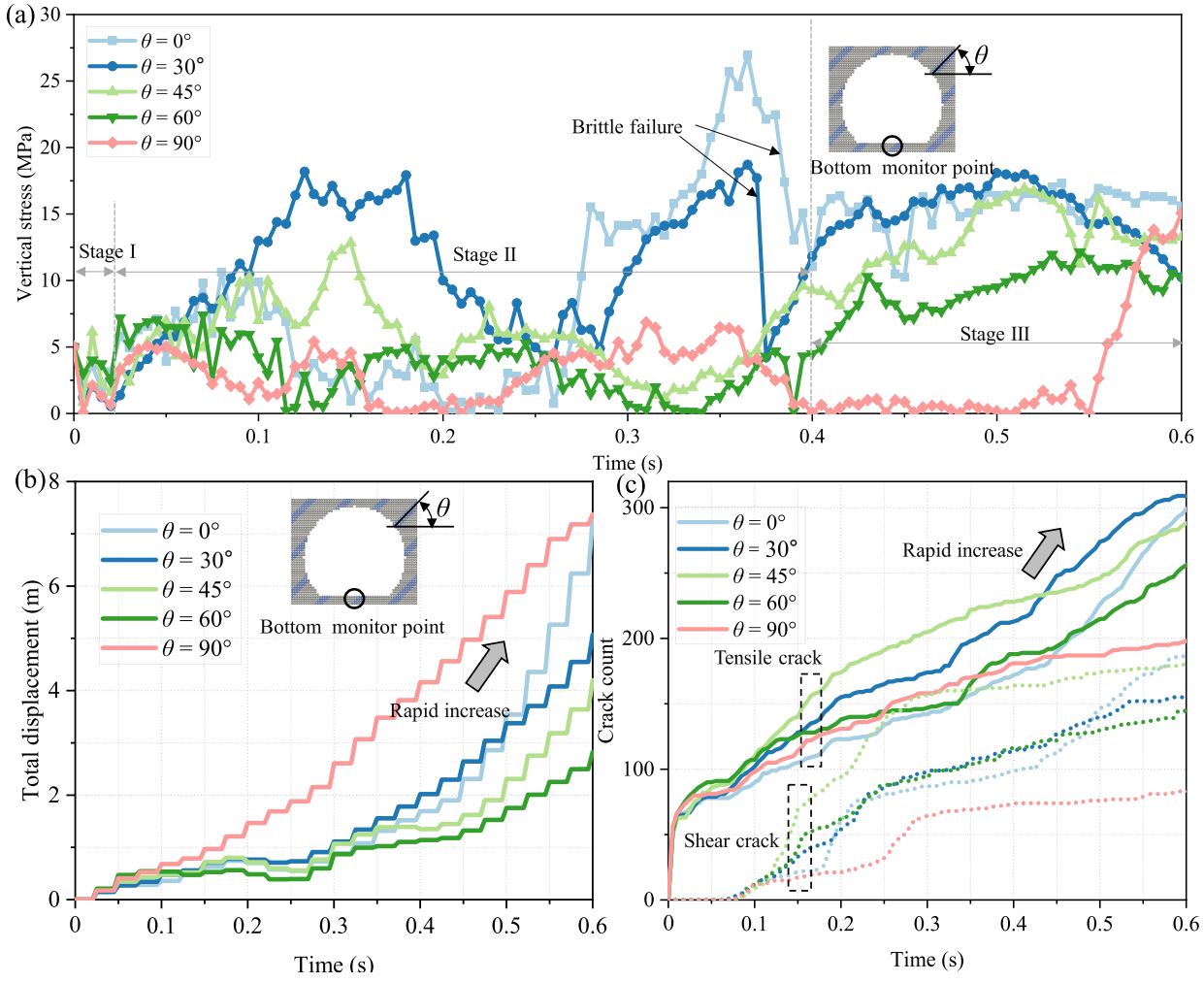

Fig. 11. Evolutions of (a) vertical stress, (b) total displacement, and (c) crack count of stratified tunnel with different θ when karst cave is located at the bottom of tunnel.

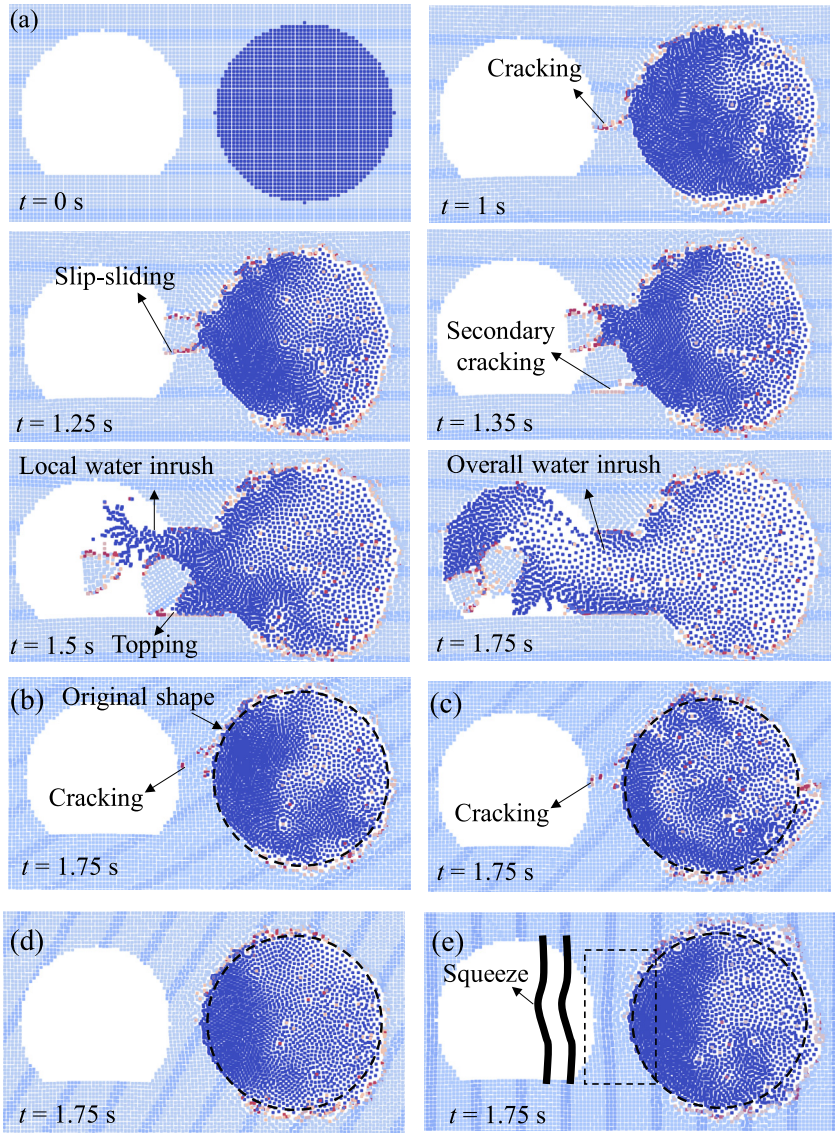

Fig. 12. Entire process of progressive rock damage and water inrush at sidewall with different dip angles. (a) $\theta = 0°$, (b) $\theta = 30°$, (c) $\theta = 45°$, (d) $\theta = 60°$, and (e) $\theta = 90°$ when karst cave is adjacent to sidewall.

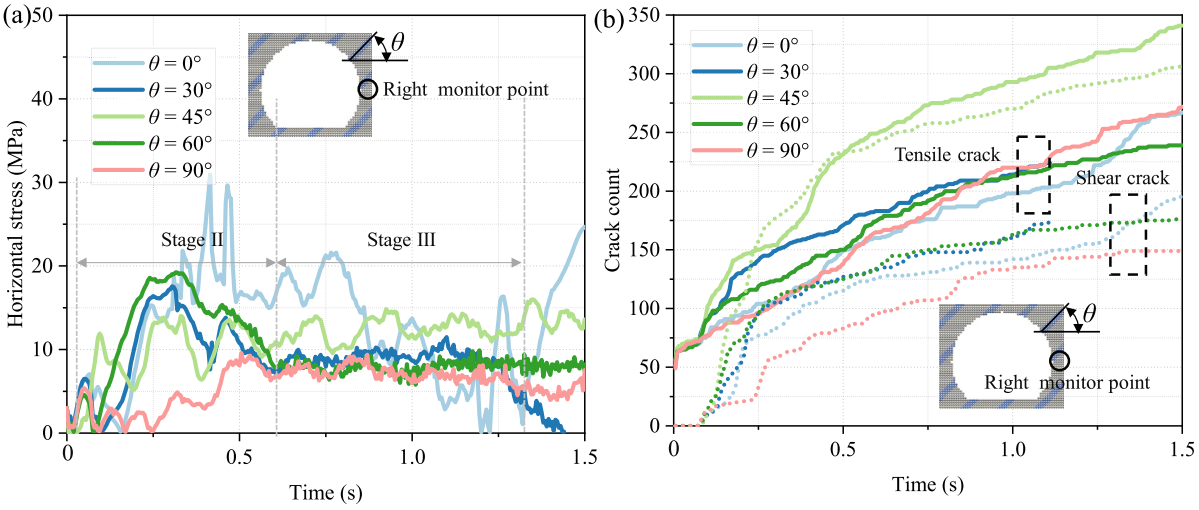

Fig. 13. Evolutions of (a) horizontal stress, and (b) crack count of the stratified tunnel with different dip angles θ when karst cave is adjacent to sidewall.

tion as illustrated by the circular dashed line in Fig. 10. This type of crack extension affects the subsequent bending failure, mainly manifested in the transformation from middle extrusion to side extrusion, which partially explains the phenomenon of water inrush and mud gushing at the bottom side of the QYS tunnel due to high dip angle bedding planes, approximately $\theta = 60°–90°$.

Quantitative comparisons of the vertical stress–strain, crack development, and displacement at the vault with different θ are presented in Fig. 11. Overall, the peak stress before rock failure in Stage II gradually increases with the increase of θ. For stratified tunnels with high dip angle bedding planes (i.e., $\theta >= 60°$), tunnel bottom simulated by SPH is prone to be unstable. Notably, the peak stress with case of $\theta = 0°$ is the highest, mainly due to the high proportion of matrix in water-resistant structure, and the weak rock breaking ability of hydraulic fracturing. This indicates that the difficulty in damaging the horizontal stratum at the top and bottom is greater than other θ. However, the accelerated movement and extensive squeeze failure in horizontal stratum caused by hydraulic fracture with high pressure result in extensive water inrush disasters. As the θ increases, the final displacement of Stages II and III gradually increases. Therefore, the stability of the bottom of the tunnel is the worst when $\theta = 60°–90°$ in rock tunnel engineering.

4.3.3 Analysis of sidewall failure and water inrush

In this section, simulated inrush processes on the sidewall (i.e., left and right position) at $t = 1.75$ s are plotted in Fig. 12. It reveals that at dip angles ranging from 30° to 90°, a stable state of the tunnel face is likely to be formed when water-filled cave exists adjacent to the sidewalls. However, at $\theta = 0°$, water-resistant rocks gradually generate shear cracks and slip along the weak layer, and the upper stratified rock of the sidewall is favorable to punching failure, culminating in a local water inrush at $t = 1.35$ s. Then the generation of secondary cracks and expansion of the lower block is formed, resulting in slip-topping failure under consistent water pressure, drag force along with friction force of the upper rock mass ($t = 1.50$ s). It is notable that some shear and tensile cracks initiate along the weak plane on sidewalls at $\theta = 30°$ and 45°. However, the shear resistance is strong enough to suppress the deformation of the structure, and the blocks of the structure can still hold horizontal pressure (Gao et al., 2023). Although no crack extension and collapse occur at $\theta = 90°$, lateral squeezing resulting from holding horizontal pressure is observed.

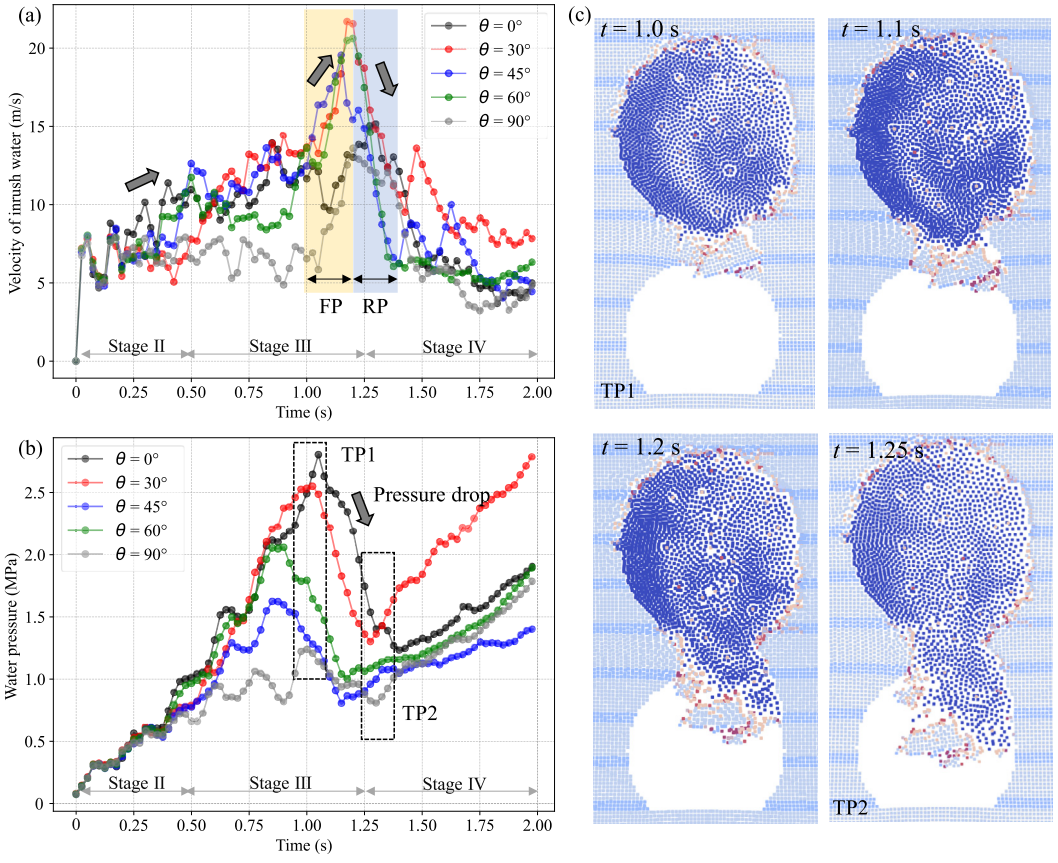

Fig. 14. Evolutions of (a) mean velocities, (b) water pressure in the cave case with different dip angles θ during the water inrush process, and (c) the failure process of stratified tunnel with $\theta = 0°$.

The corresponding horizontal stress and crack count of the sidewall are shown in Fig. 13. It is evident that during the Stage II, the peak stress of the sidewall is the highest at $\theta = 0°$ due to punching failure, while reaches the minimum value at $\theta = 90°$, primarily caused by stress release resulting from the rocks' resistance to squeezing.

5 Discussion and limitations

5.1 Discussion on the flow velocity and pressure of water inrush

The flow velocity and water pressure inside the karst cave are easily monitored on-site, allowing for the quantitative assessment of inrush disaster at various stages. In Fig. 14, the water-resistent rock undergoes a fracturing stage, with a slow increase in both mean flow velocity and water pressure during Stage II (0.05–0.50 s). As the water-resistent rock enters the block sliding stage (Stage III), the flow velocity and water pressure increase sharply until reaching a critical value, known as the turning point 1 (TP1), such as $\theta = 0°$ (2.75 MPa). Then, the water-resistent rock loosens and falls downward (Fig. 14(c), $t = 1.10$ s), resulting in the release of water pressure of karst cavities, by contrast, the flow velocity increases rapidly during the fast propagation (FP) stage. When the flow velocity reaches a peak value (PP), such as 0° (23.5 m/s), the water pressure begins decreasing until a minimum threshold (TP2), reaching 0° at 1.25 MPa. Subsequently, the rock mass enters Stage IV, where the water pressure increases in the reverse direction, and the water flow velocity gradually decreases during the recovery (RP) stage. Therefore, the variations in water pressure and flow velocity indicate the stage evolution of the inrush disaster, especially for Stages III–IV. These results indicate that once the monitored flow velocity in the field enters an FP stage or water pressure reaches a peak value (TP1), the transition from local initiation to overall inrush is faithfully predicated by the CDSPH method and immediate evacuation measures are required.

Due to the above analysis, the occurrence of PP of water pressure indicated the occurrence of overall water inrush. Therefore, the delay effect of water inrush is the most obvious with $\theta = 45°$, by contrast, the weakest delay effect is observed at $\theta = 0°$. In addition, the peak value of water pressure is also affected by different dip angles of bedding, the lowest one of 1.25 MPa with $\theta = 90°$ and the highest one of 2.82 MPa with $\theta = 0°$. We infer that the horizontal layer of water-resistant rock is stable and is not conducive to the release of water pressure, resulting in an obvious rise of water pressure and delay effect of water inrush.

The variations of water pressure and flow velocity over time for the cave located at the bottom of the tunnel are shown in Fig. 15, which exhibits a similar pattern to the water pressure and flow velocity variations during top cave inrush events. When the average water flow velocity with

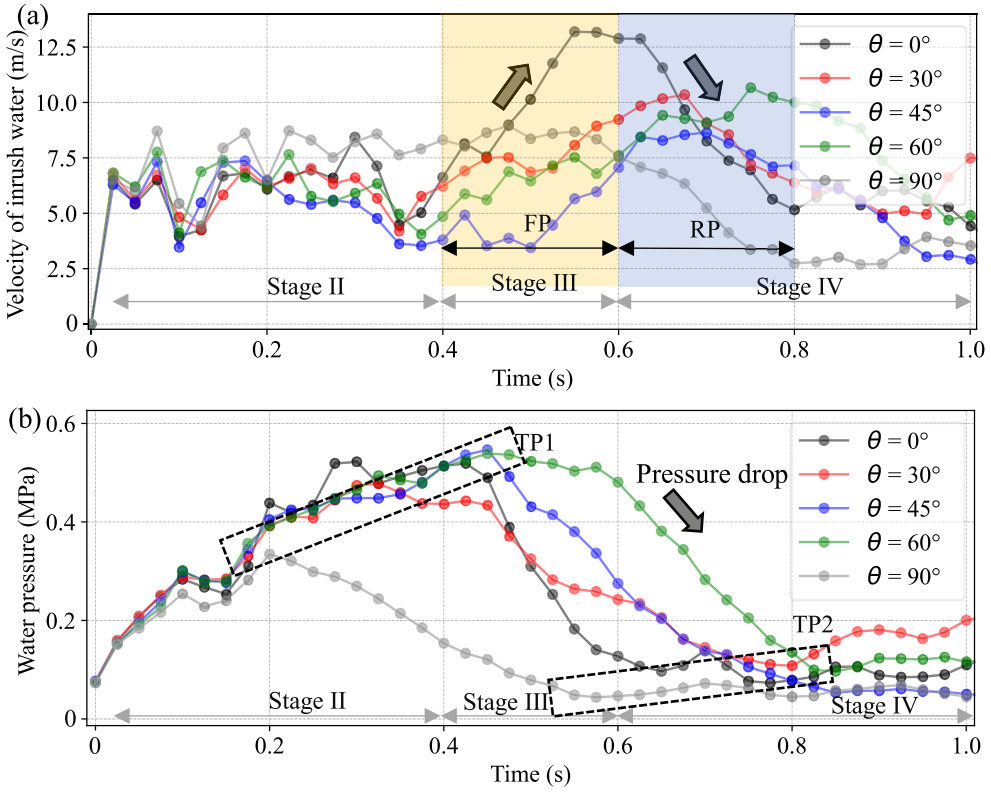

Fig. 15. Evolutions of (a) mean velocities and (b) water pressure in the cave case with different dip angles θ during the water inrush process.

$\theta = 0°$ reaches its peak value (PP) at 12.9 m/s, the water pressure starts to decrease from its peak value (TP1) to the threshold level (TP2), which indicates the overall inrush disaster. Due to the cave being situated at the bottom of the excavation face, the excavation reduces the squeezing effect of the overlying load, resulting in relatively lower water pressure compared to the situation where the cave is located at the top of the tunnel. Similar to top cave inrush events, the overall flow velocity and pressure are relatively smaller at $\theta = 90°$. However, the arrival time of Stage III is the most pronounced, and it can be deduced that for bottom-positioned karst caves, water-resistant rocks with a dip angle of 90° are more likely to induce inrush events.

The variations of water pressure and flow velocity over time for the cave located at the sidewall of the tunnel are shown in Fig. 16. The decrease in water pressure from TP1 to TP2 clearly indicates the entire process of water-resistant rock transitioning from localized contact sliding to localized gushing and finally to complete water inflow. Notably, a significant reduction in water pressure is observed for a dip angle of 0°, attributed to punching failure. For a dip angle of 45°, the hydraulic fractures of the cave propagate towards the far field of the tunnel, resulting in a relatively lower water pressure.

5.2 Compared with other cracking strategies

In contrast to other crack propagation methods such as IKSPH (Yu et al., 2021b), general particle dynamics (GPD) (Bi & Zhou, 2015; Zhou et al., 2015a), and the pseudo-spring method (Chakraborty et al., 2017; Shaw et al., 2015), CDSPH exhibits greater potential for simulating contact behavior on fracture surfaces in various appli-

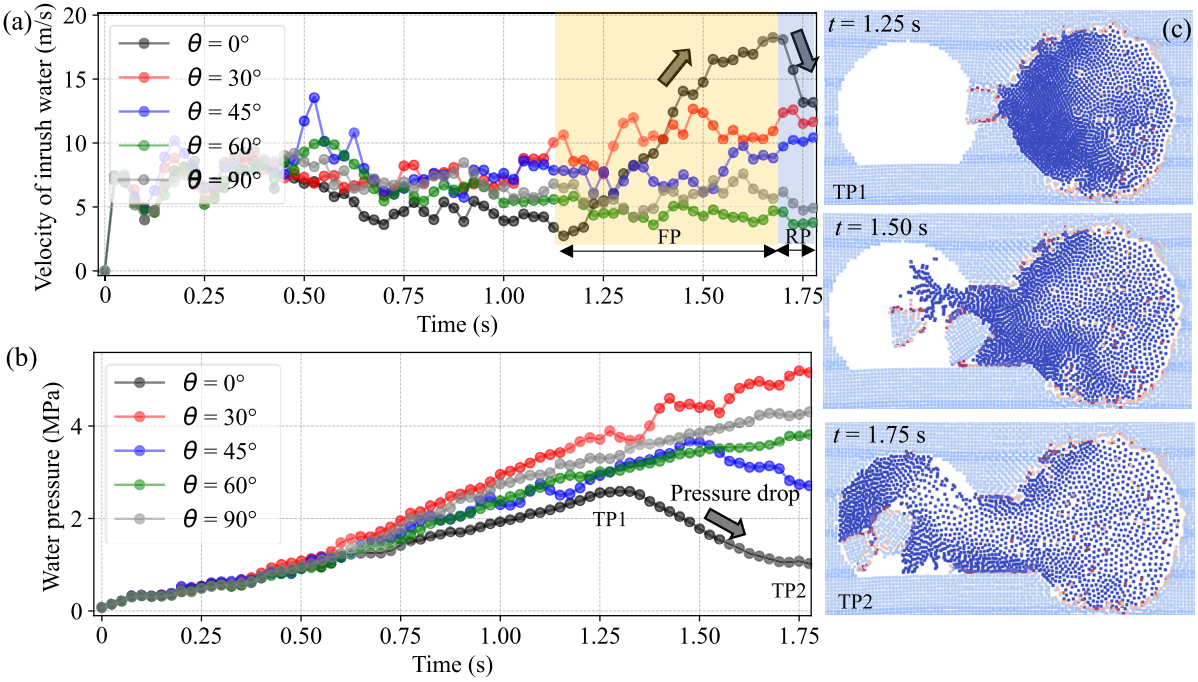

Fig. 16. Evolutions of (a) mean velocities and (b) water pressure in the cave case with different dip angles θ during the water inrush process, and (c) the failure process of stratified tunnel with $\theta = 0°$.

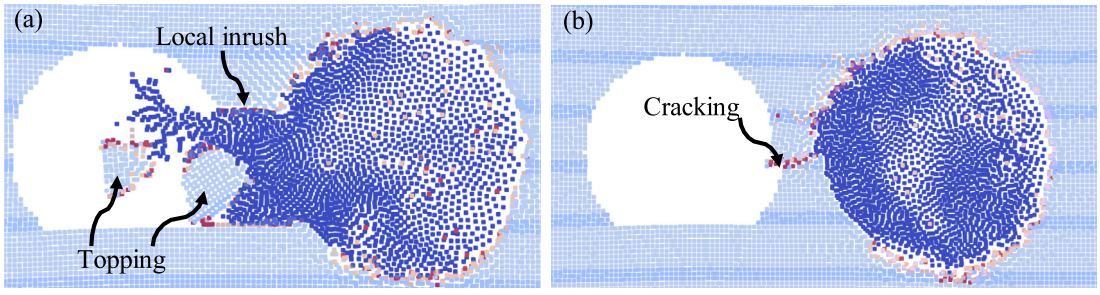

Fig. 17. Comparison result of final water inrush calculated by (a) present method (with contact algorithm), and (b) the IKSPH (Yu et al., 2021b) for modeling (without contact algorithm).

cations, including rock avalanches, excavation collapse, and foundation settlement due to the simplified contact search and contact methods (Xia et al., 2024a, 2024b). As a comparison, the results calculated by CDSPH and the IKSPH method with case $\theta = 0°$ in Section 4.3.3 are shown in Fig. 17, using identical geometrical and parameter settings. The IKSPH model exhibits overall cracking without considering contact behavior due to the direct deletion of damaged particles, providing a pathway for crack propagation (Yu et al., 2021a). However, IPs on both sides of the fracture surface still interact within the influence region of the kernel function when subjected to pressure, which results in a non-physical phenomenon of interaction on the fracture surface, as often mentioned in the pseudo-spring method (Chakraborty et al., 2017; Shaw et al., 2015). To address this defect and accurately model large deformation problems in fractured systems, DP particles arranged on the fracture surface are introduced, implementing contact algorithms that consider both normal and tangential interactions. Additionally, a reasonable SPH kernel radius is used, typically set to be $\Delta P/h$ = 0.9–1.1 to construct the fracture surface and non-continuous contact interfaces effectively (Chakraborty et al., 2017; Shaw et al., 2015). By doing so, the undesired interaction between IPs on both sides of the fracture surface under pressure is significantly reduced, thereby achieving realistic contact behavior during the block-to-block contact process. The introduction of contact algorithms into cracking models is essential for dealing with large deformation problems in fractured systems and enables a more accurate representation of the behavior of fractured materials during block-to-block interaction, toppling, and detachment processes. This enhances the overall reliability and applicability of the model for studying complex geological and engineering problems involving rock fracturing and deformation.

5.3 Limitation and future study

Based on the Mohr–Coulomb failure criterion with tensile cut-off and the explicit particle search method, the CDSPH approach can effectively simulate the cracks with high accuracy without grid re-modeling and re-meshing. However, more complex failure criteria such as the Hoek–Brown failure criterion (Hoek & Brown, 1997) need to be incorporated which are predominantly suitable for estimating the brittle fracture of rock masses.

This study utilizes the CDSPH method to model the failure process of a karst tunnel, while the weakly compressible SPH method simulates the propagation stage of water inrush. The SPH method offers an intriguing alternative for solving problems with large deformation. Conversely, mesh-based methods are better suited for problems with small deformation due to certain drawbacks associated with the SPH method, such as boundary deficiency, tensile instability, and boundary conditions. Our computational framework operates on the R9000P platform, utilizing an AMD Ryzen 7-5800H CPU paired with Radeon graphics featuring 8 cores. The CPU operates at a base frequency of 3.2 GHz, with the capability of turbo boosting up to 4.2 GHz. For a single-core, single-threaded calculation of the 2D tunnel water inrush process over 4000 steps, the computational time ranges from 35 to 45 min. There is a pressing need to augment computational power to accommodate the intricacies of three-dimensional simulation scenarios. Hence, the implementation of a GPU or CPU programming for the SPH framework is of paramount importance to enhance computational efficiency. Additionally, in order to further improve the model's computational performance, the development of multi-resolution CDSPH models will be necessary. These advancements will enable us to efficiently handle a larger number of particles while maintaining high accuracy, facilitating the simulation of more complex, large-scale and three-dimensional engineering problems in a time-efficient manner.

Moreover, this CDSPH framework is well-suited for tackling explicit dynamic problems, effectively simulating rock mass fracturing, motion, and free-surface flow of fluids. However, it currently does not account for implicit transient seepage in rock matrix and implicit seepage in joints. The former requires incorporating implicit Darcy seepage, while the latter necessitates introducing the fracture flow and non-Darcy seepage treatment. Hence, in future research, we plan to integrate the corresponding implicit seepage equations for both tunnel rock matrix and joints to better capture real-world engineering scenarios. By incorporating these additional features, the model will be enhanced to encompass the complexities of rock mass behavior, accounting for both fracturing and seepage, making it better suited to represent realistic engineering conditions. This advancement will offer a comprehensive and reliable simulation tool for a wide range of engineering applications involving fractured rock masses and fluid interactions, significantly extending the practical utility of the proposed framework.

6 Conclusions

This paper employed CDSPH method for investigating rock failure and FSI processes of QYS karst tunnel considering layer dip angles and karst cave positions. The main conclusions are detailed as:

(1) The reliability and accuracy of the CDSPH model in modeling the free surface flow, rock damage, FSI and contact between rock blocks assembly were examined and verified by hydraulic fracturing test and sliding induced impulsive wave test.
(2) The evolution of water inrush in QYS karst tunnel calculated by the CDSPH method is divided into four

stages based on vertical/horizontal stress characteristics including hydraulic fracturing of karst caves (Stage I), hydraulic fracturing of water-resistant rock (Stage II), rock sliding and local inrush (Stage III), and rock collapse and overall inrush (Stage IV).

(3) The dip angle of the weak layer planes significantly influences the hydraulic failure characteristics of water-resistant rock. When the cave is located at the top of the tunnel, the water-resistant structure with a dip angle θ of 45° poses the highest risk, while $\theta = 0°$ provides the most stability. When the cave is situated at the bottom of the tunnel, the tunnel's bottom stability is the weakest for $\theta = 60°$–$90°$ in rock tunnel engineering. When the cave is present in the sidewall of the tunnel, a dip angle of 0° leads to significant water inrush and slip-topping failure of the tunnel sidewall.

(4) The decrease in water pressure and the occurrence of maximum flow velocity within the cave can predict the transition from localized water inrush to extensive flooding, which is easily monitored on-site, allowing for the quantitative assessment of various stages for water-resistant rock failure and inrush disaster risk.

Data availability

The data that support the findings of this study are available from the corresponding author upon reasonable request.

CRediT authorship contribution statement

Chengzhi Xia: Writing – review & editing, Software, Validation, Formal analysis, Writing – original draft, Data curation, Methodology, Visualization. **Zhenming Shi:** Project administration, Writing – review & editing, Supervision, Writing – original draft. **Liu Liu:** Writing – review & editing, Supervision, Writing – original draft, Resources, Investigation. **Guangyin Lu:** Writing – review & editing, Supervision, Funding acquisition, Project administration. **Lin Zhou:** Writing – review & editing, Formal analysis, Methodology. **Chuanyi Tao:** Writing – review & editing, Investigation, Software. **Shaoqiang Meng:** Software, Writing – review & editing, Data curation, Writing – original draft, Conceptualization.

Declaration of competing interest

The authors declare that they have no known competing financial interests or personal relationships that could have appeared to influence the work reported in this study.

Acknowledgement

This research was supported by the National Natural Science Foundation for Doctoral Scholars (Grant No. 424B2055) and National Key Research and Development Program of China (Grant No. 2023YFC3008300), the National Natural Science Foundation of China (Grant Nos. 42172296 and 41974148), and the International Exchange Program for Graduate Students of Tongji University. We extend our gratitude to Professor Bo Li from Tongji University for his support with the flume experiments.

References

An, H. M., Song, Y. S., & Liu, H. Y. (2021). FDEM modelling of rock fracture process during three-point bending test under quasistatic and dynamic loading conditions. *Shock and Vibration, 2021*(1), 5566992.

Bi, J., & Zhou, X. P. (2015). Numerical simulation of zonal disintegration of the surrounding rock masses around a deep circular tunnel under dynamic unloading. *International Journal of Computational Methods, 12*(3), 150020.

Bi, J., & Zhou, X. P. (2017). A novel numerical algorithm for simulation of initiation, propagation and coalescence of flaws subject to internal fluid pressure and vertical stress in the framework of general particle dynamics. *Rock Mechanics and Rock Engineering, 50*(7), 1833–1849.

Bui, H. H., Fukagawa, R., Sako, K., & Wells, J. C. (2009). Numerical simulation of granular materials based on smoothed particle hydrodynamics (SPH). *AIP Conf. Proc., 1145*(1), 575–578.

Bui, H. H., Sako, K., Fukagawa, R., & Wells, J. C. (2008). SPH-based numerical simulations for large deformation of geomaterial considering soil-structure interaction. In *Proceedings of the 12th International Conference of International Association for Computer Methods and Advances in Geomechanics (IACMAG)* (pp. 570–578).

Chakraborty, S., Islam, M. R. I., Shaw, A., Ramachandra, L. S., & Reid, S. R. (2017). A computational framework for modelling impact induced damage in ceramic and ceramic-metal composite structures. *Composite Structures, 164*, 263–276.

Cui, W., Tang, Q. W., & Song, H. F. (2020). Washout resistance evaluation of fast-setting cement-based grouts considering time-varying viscosity using CFD simulation. *Construction and Building Materials, 242*, 117959.

Douillet-Grellier, T., Pramanik, R., Pan, K., Albaiz, A., Jones, B., Pourpak, H., & Williams, J. (2016). *Mesh-Free Numerical Simulation of Pressure-Driven Fractures in Brittle Rocks*. Texas, USA: The Woodlands.

Fang, L. F., Cao, C. M., Li, Q., Qin, K., Sun, X. D., & Ge, J. (2022). Fracture analysis of compacted clay soil beams with offset notches based on three-point bending test: Experimental characterization and numerical simulation. *Advances in Civil Engineering, 2022*(1), 3699196.

Gao, C. L., Li, L. P., Zhou, Z. Q., Li, Z. H., Cheng, S., Wang, L. G., & Zhang, D. S. (2021). Peridynamics simulation of water inrush channels evolution process due to rock mass progressive failure in karst tunnels. *International Journal of Geomechanics, 21*(4), 04021028.

Gao, J. Y., Peng, S. Y., Chen, G. Q., Mitani, Y., & Fan, H. Y. (2023). Coupled hydro-mechanical analysis for water inrush of fractured rock masses using the discontinuous deformation analysis. *Computers and Geotechnics, 156*, 105247.

Gomez-Gesteira, M., Rogers, B. D., Crespo, A. J. C., Dalrymple, R. A., Narayanaswamy, M., & Dominguez, J. M. (2012). SPHysics – development of a free-surface fluid solver – Part 1: Theory and formulations. *Computers & Geosciences, 48*, 289–299.

Gray, J. P., & Monaghan, J. J. (2004). Numerical modelling of stress fields and fracture around magma chambers. *Journal of Volcanology and Geothermal Research, 135*(3), 259–283.

Gray, J. P., Monaghan, J. J., & Swift, R. P. (2001). SPH elastic dynamics. *Computer Methods in Applied Mechanics and Engineering, 190*(49), 6641–6662.

Gui, Y., Bui, H. H., & Kodikara, J. (2015). An application of a cohesive fracture model combining compression, tension and shear in soft rocks. *Computers and Geotechnics, 66*, 142–157.

Hoek, E., & Brown, E. T. (1997). Practical estimates of rock mass strength. *International Journal of Rock Mechanics and Mining Sciences, 34*(8), 1165–1186.

Jiang, H. M., Li, L., Rong, X. L., Wang, M. Y., Xia, Y. P., & Zhang, Z. C. (2017). Model test to investigate waterproof-resistant slab minimum

safety thickness for water inrush geohazards. *Tunnelling and Underground Space Technology, 62*, 35–42.
Jin, L., Zeng, Y., Cheng, T., & Li, J. (2021). Numerical simulation of mud inrush of tunnels with coupled LBM-DEM. *Chinese Journal of Geotechnical Engineering, 43*(6), 1000–1009 (in Chinese).
Lai, Y. B., Li, S., Guo, J. Q., Zhu, Z. G., & Huang, X. (2021). Analysis of seepage and displacement field evolutionary characteristics in water inrush disaster process of karst tunnel. *Geofluids, 2021*, 5560762.
Li, H. Y., Xu, H. B., Li, Z. F., Li, H. W., Zhang, H. J., Zhang, Y. J., & Chang, T. (2018). Study on treatment of fault water gushing in deep roadway. *Journal of Mining & Safety Engineering, 35*(3), 635–641 (in Chinese).
Li, L. P., Sun, S. Q., Wang, J., Song, S. G., Fang, Z. D., & Zhang, M. G. (2020). Development of compound EPB shield model test system for studying the water inrushes in karst regions. *Tunnelling and Underground Space Technology, 101*, 103404.
Li, S. C., Yuan, Y. C., Li, L. P., Ye, Z. H., & Lei, T. (2015). Water inrush mechanism and minimum safe thickness of rock wall of karst tunnel face under blast excavation. *Chinese Journal of Geotechnical Engineering, 37*(2), 313–320 (in Chinese).
Lian, Y. J., Bui, H. H., Nguyen, G. D., & Haque, A. (2023). An effective and stabilised ($\mathbf{u}$–p_l) SPH framework for large deformation and failure analysis of saturated porous media. *Computer Methods in Applied Mechanics and Engineering, 408*, 115967.
Liang, D. X., Jiang, Z. Q., Zhu, S. Y., Sun, Q., & Qian, Z. W. (2016). Experimental research on water inrush in tunnel construction. *Natural Hazards, 81*(1), 467–480.
Lucy, L. B. (1977). A numerical approach to the testing of the fission hypothesis. *The Astronomical Journal, 82*, 1013–1024.
Molteni, D., & Colagrossi, A. (2009). A simple procedure to improve the pressure evaluation in hydrodynamic context using the SPH. *Computer Physics Communications, 180*(6), 861–872.
Monaghan, J. J. (2000). SPH without a Tensile Instability. *Journal of Computational Physics, 159*(2), 290–311.
Monaghan, J. J. (2005). Smoothed particle hydrodynamics. *Reports on Progress in Physics, 68*(8), 1703–1759.
Mu, D. R., Wen, A. H., Zhu, D. Q., Tang, A. P., Nie, Z., & Wang, Z. Y. (2022). An improved smoothed particle hydrodynamics method for simulating crack propagation and coalescence in brittle fracture of rock materials. *Theoretical and Applied Fracture Mechanics, 119*, 103355.
Peng, X. Y., Yu, P. C., Cheng, X., Chen, G. Q., Zhang, Y. B., Zhang, H., & Li, C. Z. (2022). Dynamic simulation of the water inrush process in tunnel construction using a three-dimensional coupled discontinuous deformation analysis and smoothed particle hydrodynamics method. *Tunnelling and Underground Space Technology, 127*, 104612.
Qian, Q. H., & Lin, P. (2016). Safety risk management of underground engineering in China: Progress, challenges and strategies. *Journal of Rock Mechanics and Geotechnical Engineering, 8*(4), 423–442.
Shaw, A., Reid, S. R., Roy, D., & Chakraborty, S. (2015). Beyond classical dynamic structural plasticity using mesh-free modelling techniques. *International Journal of Impact Engineering, 75*, 268–278.
Sheikh, B., Qiu, T., & Ahmadipur, A. (2021). Comparison of SPH boundary approaches in simulating frictional soil–structure interaction. *Acta Geotechnica, 16*(8), 2389–2408.
Shu, Q., Wang, X. B., Zhao, Y. F., & Bai, X. Y. (2020). Numerical simulation of failure processes of heterogeneous rock specimens under assumption of invariant spherical stress during stress drop. *Rock and Soil Mechanics, 41*(10), 3465–3472 (in Chinese).
Vacondio, R., Mignosa, P., & Pagani, S. (2013). 3D SPH numerical simulation of the wave generated by the Vajont rockslide. *Advances in Water Resources, 59*, 146–156.
Wang, J., Zhang, Y., Qin, Z., Song, S. G., & Lin, P. (2020). Analysis method of water inrush for tunnels with damaged water-resisting rock mass based on finite element method-smooth particle hydrodynamics coupling. *Computers and Geotechnics, 126*, 103725.
Wang, X. T., Li, S. C., Xu, Z. H., Hu, J., Pan, D. D., & Xue, Y. G. (2019). Risk assessment of water inrush in karst tunnels excavation based on normal cloud model. *Bulletin of Engineering Geology and the Environment, 78*(5), 3783–3798.
Williams, P. W. (2008). The role of the epikarst in karst and cave hydrogeology: A review. *International Journal of Speleology, 37*(1), 1–10.
Wu, J., Li, S. C., Xu, Z. H., & Zhao, J. (2019). Determination of required rock thickness to resist water and mud inrush from karst caves under earthquake action. *Tunnelling and Underground Space Technology, 85*, 43–55.
Xia, C. Z., Shi, Z. M., & Li, B. (2024a). A modified SPH framework of for simulating progressive rock damage and water inrush disasters in tunnel constructions. *Computers and Geotechnics, 167*, 106042.
Xia, C. Z., Shi, Z. M., & Li, B. (2024b). A revisit of disaster process of Vajont rockslide using a coupled discontinuous smooth particle hydrodynamics (CDSPH) method. *Landslides, 21*(1), 197–216.
Xia, C. Z., Shi, Z. M., Li, B., Zheng, H. C., & Liu, M. M. (2022). Verification and application of an improved smooth particle hydrodynamics method for a rock slope under seismic conditions. *Earth Science, 47*(12), 4469–4483 (in Chinese).
Xia, C. Z., Shi, Z. M., Liu, M. M., Li, B., Yu, S. B., & Xue, J. F. (2024c). Dynamic analysis of field-scale rockslides based on three-dimensional discontinuous smoothed particle hydrodynamics: A case study of Tangjiashan rockslide. *Engineering Geology, 336*, 107558.
Xia, C. Z., Shi, Z. M., & Zheng, H. C. (2023). An improved smooth particle hydrodynamics method for modelling crack propagation in layered rock cells and slopes. *Bulletin of Engineering Geology and the Environment, 82*(4), 129.
Xie, Q., Cao, Z. L., Sun, W. C., Fumagalli, A., Fu, X., Wu, Z. H., & Wu, K. (2023). Numerical simulation of the fluid-solid coupling mechanism of water and mud inrush in a water-rich fault tunnel. *Tunnelling and Underground Space Technology, 131*, 104796.
Xu, D. P., Feng, X. T., Chen, D. F., Zhang, C. Q., & Fan, Q. X. (2017). Constitutive representation and damage degree index for the layered rock mass excavation response in underground openings. *Tunnelling and Underground Space Technology, 64*, 133–145.
Xu, W. J., Wang, Y. J., & Dong, X. Y. (2021a). Influence of reservoir water level variations on slope stability and evaluation of landslide tsunami. *Bulletin of Engineering Geology and the Environment, 80*(6), 4891–4907.
Xu, Z. H., Lin, P., Xing, H. L., Pan, D. D., & Huang, X. (2021b). Hydro-mechanical Coupling Response Behaviors in Tunnel Subjected to a Water-Filled Karst Cave. *Rock Mechanics and Rock Engineering, 54*(8), 3737–3756.
Yan, C. B., Xu, G. Y., & Zuo, Y. J. (2006). Destabilization analysis of overlapping underground chambers induced by blasting vibration with catastrophe theory. *Transactions of Nonferrous Metals Society of China, 16*(3), 735–740.
Yu, S. Y., Ren, X. H., Zhang, J. X., Wang, H. J., & Sun, Z. H. (2021a). An improved form of smoothed particle hydrodynamics method for crack propagation simulation applied in rock mechanics. *International Journal of Mining Science and Technology, 31*(3), 421–428.
Yu, S. Y., Ren, X. H., Zhang, J. X., Wang, H. J., & Sun, Z. H. (2021b). An improved smoothed particle hydrodynamics method and its application in rock hydraulic fracture modelling. *Rock Mechanics and Rock Engineering, 54*(12), 6039–6055.
Zhan, L., Peng, C., Zhang, B. Y., & Wu, W. (2020). A SPH framework for dynamic interaction between soil and rigid body system with hybrid contact method. *International Journal for Numerical and Analytical Methods in Geomechanics, 44*(10), 1446–1471.
Zhang, T., Gan, Q., Zhao, Y. X., Zhu, G. P., Nie, X. D., Yang, K., & Li, J. Z. (2019). Investigations into mining-induced stress–fracture–seepage field coupling effect considering the response of key stratum and composite aquifer. *Rock Mechanics and Rock Engineering, 52*(10), 4017–4031.
Zhou, X. P., Wang, Y. T., Shou, Y. D., & Kou, M. M. (2018). A novel conjugated bond linear elastic model in bond-based peridynamics for fracture problems under dynamic loads. *Engineering Fracture Mechanics, 188*, 151–183.
Zhou, X. P., Zhao, Y., & Qian, Q. H. (2015a). Numerical simulation of rock failure process in uniaxial compression using smoothed particle hydrodynamics. *Chinese Journal of Rock Mechanics and Engineering, 34*, 2647–2658 (in Chinese).
Zhou, X. P., Wang, Y. T., & Qian, Q. H. (2016). Numerical simulation of crack curving and branching in brittle materials under dynamic loads using the extended non-ordinary state-based peridynamics. *European Journal of Mechanics – A/Solids, 60*, 277–299.

Zhou, X. P., Zhao, Y., & Qian, Q. H. (2015b). A novel meshless numerical method for modeling progressive failure processes of slopes. *Engineering Geology, 192*, 139–153.

Zhou, Z. Q., Li, L. P., Shi, S. S., Liu, C., Gao, C. L., Tu, W. F., & Wang, M. X. (2020). Study on tunnel water inrush mechanism and simulation of seepage failure process. *Rock and Soil Mechanics, 41*(11), 3621–3631 (in Chinese).

Zhu, W. C., & Wei, C. H. (2011). Numerical simulation on mining-induced water inrushes related to geologic structures using a damage-based hydromechanical model. *Environmental Earth Sciences, 62*(1), 43–54.